Texture-dependent all-optical switching in ferromagnetic films via stochastic nucleation of nanoscale domains

Dinar Khusyainov[1*], Rein Liefferink[1], MengXing Na[1], Fabian Kammerbauer[2], Robert Frömter[2], Mathias Kläui[2], Dmitry Kozodaev[3], Nikolay Vovk[4], Rostislav Mikhaylovskiy[4], Dmytro Afanasiev[1], Alexey Kimel[1], Johan H. Mentink[1], Theo Rasing[1]

[1*]*Institute for Molecules and Materials, Radboud University, Nijmegen, 6525 AJ, Netherlands.*
[2]*Institute of Physics, Johannes Gutenberg University Mainz, Mainz, 55099, Germany.*
[3]*NT-MDT BV, Sutton 11A, Apeldoorn, 7327AB, Netherlands.*
[4]*Department of Physics, Lancaster University, Bailrigg, Lancaster, LA1 4YW, United Kingdom.*

*Corresponding author. E-mail: dinar.khusyainov@ru.nl;

Controlling magnetic textures at ever smaller length and time scales is of key fundamental and technological interest. Achieving nanoscale control often relies on finding an external stimulus that is able to act on that small length scale, which is highly challenging. A promising alternative is to achieve nanoscale control using the inhomogeneity of the magnetic texture itself. Using a multilayered ferromagnetic Pt/Co/Pt thin-film structure as a model system, we employ a magnetic force microscope to investigate the formation of homogeneous magnetization induced by circularly polarized picosecond laser pulses. We observe the stochastic nucleation of complex nanotextured domains from an initially saturated magnetic state. Illuminating these domains with circularly polarized light results in deterministic and homogeneous switching of the magnetization. The growth of nanotextured domains depends not only on their macroscopic magnetization but also on the complexity of the texture. This helicity and texture-dependent effect contrasts with the typical homogeneous growth of magnetic domains initiated by an effective magnetic field of a circularly polarized laser pulse. We corroborate our findings with a stochastic model for the nucleation of magnetic domains, in which the nucleation and annihilation probability not only depends on the helicity of light but also on the relative magnetization orientation of neighboring domains. Supported by stochastic modeling, our observations reveal the key mechanisms underlying the multipulse nature of helicity-dependent all-optical switching in ferromagnetic thin films.

Introduction

Femtosecond laser pulses have led to a plethora of new and unexpected realizations of phase transitions between different crystallographic [1–6], electronic [7–11], or magnetic order [12–19] that can be controlled on ultrafast timescales. While these phase transitions have been extensively studied, it remains challenging to discern how ultrafast phase transitions occur at the nanoscale. In this regard, ultrafast phase transitions characterized as "first-order" in equilibrium are particularly interesting. Examples include the metal-to-insulator transition [3, 20, 21], reversal of ferroelectric polarization [22], as well as transition to a hidden electronic state [23, 24]. These first-order phase transitions feature hysteresis and phase coexistence. Therefore, nanoscale (meta)stable domains of one phase can be photo-induced inside the pre-existing stable phase on an ultrafast time scale. Recent studies indicate that the inherent stochasticity of the domain nucleation is essential for understanding the transition pathway [3, 25]. Additionally, recent studies on laser-induced topological phase transitions involving the stochastic formation of nanoscale skyrmions [14] were shown to rely on fluctuations. Therefore, a deeper understanding of the control of such photo-induced stochasticity is of key interest.

Distinct from structural and electronic, magnetic phase transitions offer an additional degree of freedom due to the dependence of the light-spin interaction on the helicity of light. This has been widely exploited for transparent magnetic media based on the ultrafast inverse Faraday effect [26–28]. Moreover, in metallic magnets, magnetic circular dichroism (MCD) can be utilized to control the magnetic state [29–32]. It has been suggested that the control of magnetization with circularly polarized light depends on the local magnetization or the difference in the absorption of circularly polarized light between two oppositely oriented magnetic domains. The latter can cause domain wall motion induced by a thermal gradient across the domain wall [30, 33–36]. Such all-optical control has been associated with the emergence of sub-micrometer magnetic domains [33, 35, 37]. The

formation of these nanoscale domains aligns with the physics of first-order phase transitions, where phase coexistence and nucleation processes play a crucial role. However, direct experimental evidence of helicity-dependent manipulation of nanoscale magnetic textures remains elusive [38].

Studying the effect of circularly polarized light on photo-induced magnetic nanotextures requires observing nanoscale changes after exposure to picosecond laser pulses. This is a challenging task where conventional optical microscopy fails due to the fundamental diffraction limit. Magnetic force microscopy (MFM) is a tabletop technique that can solve these challenges. MFM is a well-established and widely used technique because of its high spatial resolution (~10 nm) and simplicity [39, 40]. Indeed, MFM has enabled the study of magnetic domain walls [41] and topological magnetic particles such as vortices [42], skyrmions [43, 44], and even merons [45]. Moreover, MFM has also been recently employed to study nanotextures induced after all-optical switching in ferrimagnetic Tb/Fe multilayers [46].

Here, we employ MFM to study the laser-induced magnetic domain nanotexture in helicity-dependent switching in a ferromagnetic trilayer Pt/Co/Pt. Our measurements reveal that consistent with the established physics of first-order phase transitions, the first few laser pulses trigger the stochastic nucleation of sub-micrometer magnetic domains. By systematically studying the evolution of the photo-induced magnetic nanotexture of the micrometer and sub-micrometer domains as a function of the number of circularly polarized incident pulses, we find that the complexity of the nanotexture of these domains evolves differently than the total switched area. Moreover, by varying the laser fluence, we are able to distinguish between the nucleation and heating of the magnetic nanotextured domains. In particular, we demonstrate that under the action of laser radiation, isolated sub-micrometer domains shrink instead of grow. Both these findings show that existing mechanisms for all-optical magnetization switching, which rely on an effective magnetic field originating from the inverse Faraday effect [47, 48] or a temperature gradient-driven domain wall motion [33, 34, 49], are not able to describe the effect of picosecond circularly polarized laser pulses on magnetic nanotextured domains. To explain our experimental results, we developed a phenomenological model based on switching energy barriers of the nanoscale domains that account for the MCD effect and depend on the relative orientation of adjacent domains, achieving effective domain growth via nucleation and coalescence.

Results

The sample we studied is a ferromagnetic Pt/Co/Pt trilayer with perpendicular magnetic anisotropy (as shown in Fig. 1a). We first establish the necessary conditions for laser-induced deterministic switching of magnetization in our sample using conventional magneto-optical microscopy. In our experiments, we utilize circularly polarized laser pulses with specific helicities chosen to achieve deterministic switching (see the Methods section). The pulse duration is set to 3 picoseconds, as this duration provides the highest efficiency for multipulse helicity-dependent control of magnetization, consistent with previous experiments conducted on Co/Pt samples [30, 33–35, 37].

A sketch of the phase diagram of the magnetization state (M) after illumination with circularly polarized pulses as a function of the number of pulses (N) and fluence is presented in Fig. 1b. First, we observe that above a fluence of F_T = 2.6 mJ/cm^2, the sample can't be switched deterministically. Below this threshold, the ferromagnetic monodomain ground state shifts to deterministic switching through an intermediate state with partial switching as N increases. At least ten pulses are needed here to achieve deterministic switching; however, adding more pulses turns the deterministic switching state into a mixed state of partial and deterministic switching.

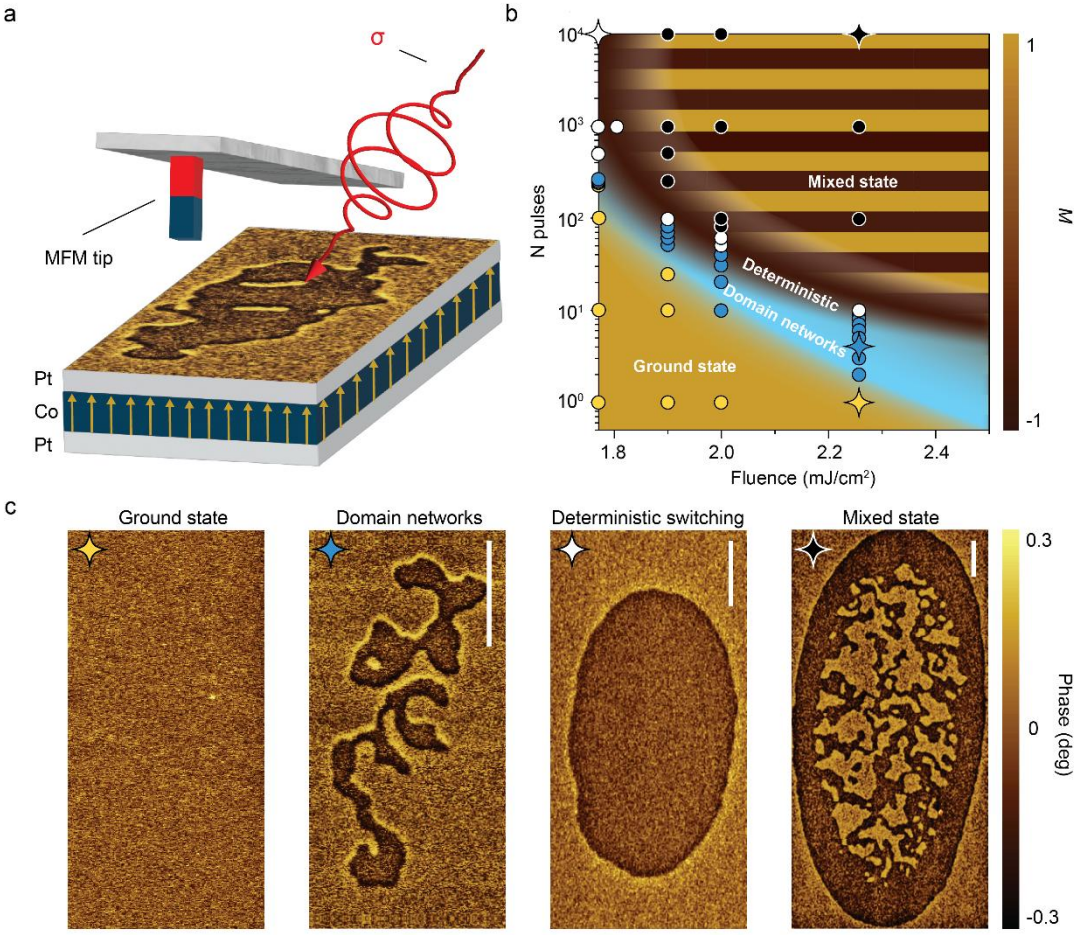

Fig. 1 Nanoscopy of the magnetic nanotextures in Pt/Co/Pt trilayers. (a) Sketch of the in situ MFM measurement of domains nucleated by picosecond circularly polarized (σ) laser pulses in Pt/Co/Pt trilayers. Arrows indicate spins that are aligned in the direction perpendicular to the surface plane. **(b)** Sketch of the phase diagram of the magnetization state M as a function of the number N of circularly polarized laser pulses and fluence. The magnetization, denoted as M =1 and M =−1, represents the magnetization directions "up" and "down," respectively. The diagram of the laser-induced magnetization has been reconstructed using data obtained from Faraday microscopy and MFM (original data can be found in Extended Data Fig. 1 and Supplementary material 1). The data points illustrate sampled phase boundaries, displaying the ground state (yellow data points), domain networks (blue data points), deterministic switching (white data points) and mixed state (black data points). Blue area extrapolated according to the MFM data. **(c)** MFM images of typical nanotextured domains observed in the deterministic switching, mixed state, and domain networks state. The scale bar is 5 µm.

To achieve nanometer-scale resolution, we aligned the laser to the scanning region of the MFM tip and performed *in situ* probing of the laser-induced nanotextured magnetic domains (Fig. 1a). Using MFM, we discovered that the intermediate partially switched state (the light-blue region in Fig. 1b) is characterized by interconnected domains, which we term domain networks. As these domain networks are typically of micrometer size, the resolution of MFM allows us to resolve the nanoscale texture of these domains. Typical MFM images displaying the magnetic domains observed in the deterministic switching, domain networks, and mixed states are presented in Fig. 1c. We provide a complete data set of magneto-optical and MFM images that support the phase diagram in Extended Data Fig. 1 and Supplementary material 1.

Next, we focus on the evolution of the domain networks under the action of different numbers of pulses. In our experiments, we use sequences of the millisecond-separated pulses in the range from 0 to 10 pulses, each having a fluence $F = 2.26$ mJ/cm^2. A representative evolution of the nucleated magnetic nanotextures as a function of N of circularly polarized laser pulses is shown in Fig. 2a. We repeated the experiment three times for each N value. After each MFM image, the irradiated region was returned to its ground state using an external magnetic field higher than the coercive field of the sample (see the Methods section). We observe that already, after two pulses, domains having a size of about 1-2 µm are generated. After four pulses, the nucleated domains coalesce into domain networks. Although the total switched area remains roughly the same in each repetition of the

experiment, the locations and forms of the nucleated domains vary across the illuminated spot. With an increased number of pulses, we observe an increased coalescence of the domain networks, resulting in nearly uniformly switched magnetization after about ten pulses.

To quantify our observations, we use two metrics. The first is the switched area (A_s), normalized by the total area of the laser beam (A_b). As shown in Fig. 2b, the growth of the A_s/A_b is approximately linear in the range of 10 pulses, as indicated by the solid grey line. Secondly, we measure the complexity of the domain network texture using the fractal dimension D as a parameter calculated via the Minkovski-Bouligand method [50, 51], see Extended Data Fig. 4. We treat the domain wall as a one-dimensional object so that a fractal dimension $D = 1$ would refer to perfectly round domains. Fig. 2b shows the rapid growth of the domain's complexity when N varies from 2 to 6. One can see that during this stage, the nucleated domains begin to coalesce, forming domain networks. At 6 pulses, D peaks at a value of ~1.24, where we see the most complex texture of magnetic domains. After six pulses, the fractal dimension D levels off, indicating that the domain texture evolves towards a deterministic switching state. Subsequently, illuminating the sample with up to 100 pulses with $F = 2.26$ mJ/cm^2 leads to the development of a mixed state. After 1000 pulses, the separation between deterministic state and domain networks in the mixed state becomes apparent with the switched ring and smooth domain wall, where D equals 1.15 (See Extended Data Fig. 2.). The main cause of the mixed state's emergence is the heat accumulation in the center of the illuminated area [37]. We estimate the heat accumulation and its spatial distribution in our sample, as detailed in Supplementary Notes 4, 5. The effect of accumulated heating on switching is demonstrated in Supplementary Note 6.

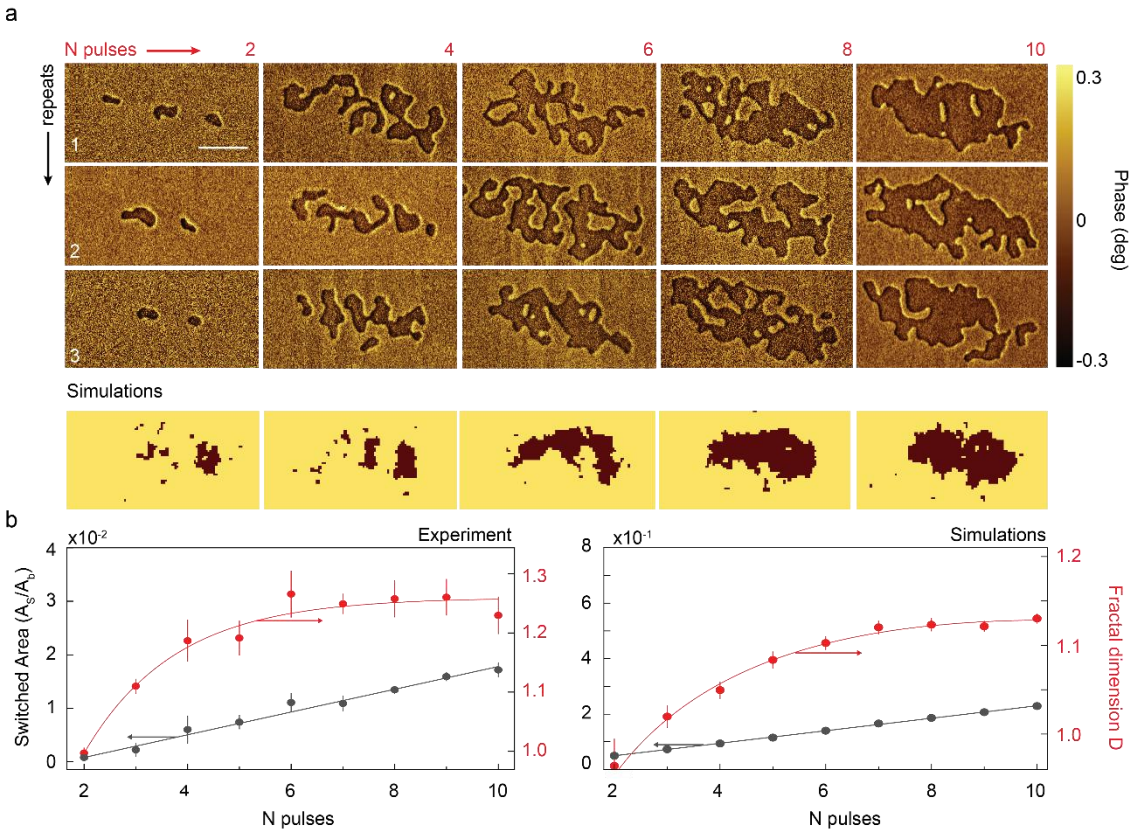

Fig. 2 Multi-pulse evolution of stochastic domain networks. **(a)** MFM images of the laser-induced stochastic domain networks as a function of the number of pulses N at a fluence of $F = 2.26$ mJ/cm^2. The lower panel shows the result of the simulations using a probabilistic energy barrier-based model (details, see below). The scale bar is 5 µm. **(b)** The normalized switched area A_s/A_b (gray) and the fractal dimension D (red) as a function of the incident number of circularly polarized laser pulses N, calculated from the experiments and simulations, respectively. The solid lines serve as a guide for the eye. The switched area grows linearly up to 10 pulses, as seen in the experiments and simulations. In D, we observe a rapid increase to $D \sim 1.24$ (~1.12) from 0 to 6 pulses, followed by a plateau for experiments and simulations.

The observed multi-pulse formation of the domain networks deviates from the established understanding of deterministic switching in Co/Pt multilayers. The conventional models explain all-optical switching in ferromagnetic thin films as nucleation followed by the gradual growth of domains, driven by temperature differences across domain walls [30, 33–35]. This gradient arises from the MCD effect across a domain wall caused by differences in absorbed laser power for domains with opposite directions of magnetization. The subsequent temperature difference drives the domain wall from the colder toward the hotter region. For instance, temperature gradients on the order of $\nabla T = 1$ K/nm have been reported [33–35, 52]. It remains uncertain whether the temperature gradient also plays a dominant role in deterministic switching at the nanoscale. In this scenario, we would expect a steady-state growth of domains with each laser pulse, resulting in growth that is uniformly distributed along the entire domain wall. This should maintain the complexity of the nucleated domains. However, this expectation contrasts sharply with the results of our experiments.

We conducted the following experiment to investigate the contribution of the MCD-derived domain wall motion to the deterministic switching process at the nanoscale. Using the fluence F_T, we first nucleate a set of mutually isolated domains, see Fig. 3. Next, we illuminate the nucleated domains with identical pulses but with a fluence below F_T, thus prohibiting further nucleation of the domains. This allows us to investigate the growth of the existing domains solely. As circularly polarized pulses are more strongly absorbed by the ground state, the temperature is higher outside the sub-micrometer isolated domains, and thus, the domains are expected to grow. In contrast to these expectations, Fig. 3 shows that at F=2.4 mJ/cm^2 < F_T, nucleated domains became smaller with each subsequent pulse until the third below-threshold pulse annihilated them. These observations prove that an effective magnetic field originating from the MCD-induced thermal gradient is not the dominant mechanism at

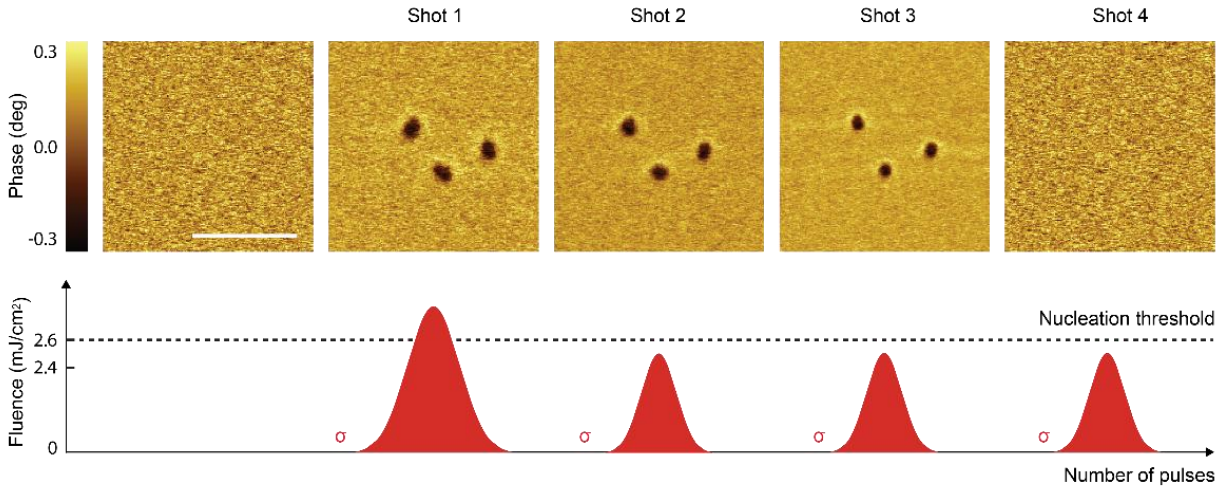

Fig. 3 Evolution of photo-induced sub-micrometer domains under the MCD-derived temperature gradient. First, a pulse with above threshold fluence (2.6 mJ/cm^2) was used to nucleate sub-micrometer domains. The fluence of subsequent pulses was reduced to 2.4 mJ/cm^2 to prevent additional nucleation. We observe the shrinking and eventual annihilation of the nucleated domains. The scale bar is 5 µm.

the nanoscale. Hence, the impact of circularly polarized light on the observed sub-micrometer magnetic domains has to be attributed to another microscopic mechanism.

Discussion

To explain our experimental observations, we propose a phenomenological model that can be seen as an extension of the model for granular magnetic media developed by Gorchon *et al.* [31, 32]. To adapt this model to the case of continuous films, we consider a system composed of small domains, where each domain is defined by either magnetization up or down, denoted as $M = \pm 1$. For simplicity, we choose an equidistant mesh in two dimensions, in which each cell has the same size, corresponding to the smallest stable domain observed experimentally (see Extended Data Fig. 9). Following Gorchon *et al.*, the effect of the laser pulse is modeled as an Arrhenius activation over an energy barrier. In this model, the characteristic time for the system to transition over the energy barrier is expressed as $\tau = \tau_0 exp(E_b/k_B T)$, where E_b is the energy barrier, T is the electronic temperature, and $1/\tau_0$ represents the attempt frequency to overcome the barrier [31]. Distinct from granular systems, we introduce a dependence on the alignment of the adjacent domains in the switching energy barrier for continuous films. As shown in the Supplementary Note 2, it follows from micromagnetic calculations that the dependence takes the form

$$E_b(n) = E_0 + E_1 n, \tag{1}$$

where $0 \leq n \leq 4$ represents the number of direct neighbors of the cell aligned parallel to it. In short, the energy barrier is reduced by the presence of domain walls with neighboring domains, leading to a linear dependence on the number of aligned neighbors. To model the dynamical changes of the domains under the influence of laser pulses, we assume that the switching probability during a short time interval $\Delta t \ll \tau$ is given by $P = \Delta t/\tau$.

We simulate the experiment by iterating over the time step Δt. Ultrashort laser pulses are treated as temporal and spatial temperature profiles that act as ultrafast heating and exponential heat dissipation. The details of this are provided in the Methods section. The MCD due to circularly polarized laser pulses is implemented such that the $M = 1$ grid cells (yellow) experience a 4% higher laser heating than the $M = -1$ cells (black). The results of this simulation are shown in Fig. 2, next to the MFM measurements discussed earlier. We see that the model exhibits qualitative agreement with the experimental observations. Using this model, we can also explain how the mixed state forms and how the helicity of light affects the laser-induced evolution of stochastic domain networks (See Extended Data Fig. 2 and Extended Data Fig. 3).

To better understand the physics of this model and particularly the role of MCD, we illustrate it for a simple system. Fig. 4a shows the energy barriers for a single domain as a function of the number of aligned neighbors. When no neighbors are aligned, the domain exhibits the lowest energy barrier and the highest switching probability. As the number of aligned neighbors grows, the barrier increases, and the switching probability decreases. Upon introducing the small temperature differences caused by the MCD, denoted as $\pm\Delta T$ (for M=±1, respectively), the switching probabilities $P(n)$ are affected by $P_\sigma(n) - P(n)$, where $P_\sigma(n)$ is the probability at T

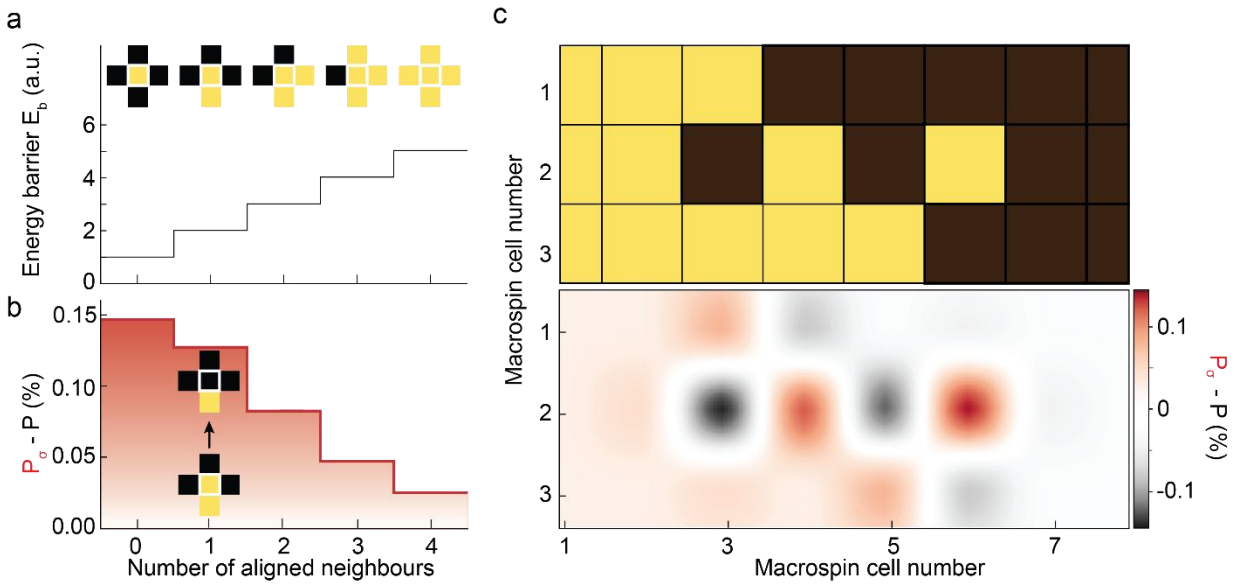

Fig. 4 The impact of the texture and helicity of light on the switching probability. **(a)** Energy barriers of the single M =1 (yellow) cell as a function of the aligned nearest neighbors. **(b)** Difference between switching probabilities with and without MCD as a function of aligned nearest neighbors at peak temperature (see Eq. (2)). The effect is maximized for zero and one aligned neighbor. The background color represents the color bar from Fig 4c. **(c)** The macrospin model is calculated for a small grid of cells (top). The enhancement of the switching probability due to the MCD effect close to the complex domain wall is shown at the bottom. The bottom panel is a sketch that doesn't represent the actual resolution.

$\pm \Delta T$ caused by circularly polarized light. As illustrated in Fig. 4b, the size of this change depends on the number of aligned neighbors n of a given cell (at the maximum temperature reached in the simulation). To understand this point, we perform a linearization in $\Delta T/T$

$$P_\sigma(n) - P(n) \propto M \cdot exp\left(-\frac{E_0+E_1 n}{k_B T}\right) \cdot \frac{E_0+E_1 n}{k_B T} \cdot \frac{\Delta T}{T}. \quad (2)$$

In the simulation parameters, the condition $(E_0 + E_1 n)/(k_B T) \geq 1$ is satisfied. This ensures that the exponential decay dominates over the linear term, decreasing $P_\sigma(n) - P(n)$ as n increases. This observation explains why the MCD-derived enhancement of switching probability is most significant for cells with no or one aligned neighbor. We simulate a complex magnetic nanotexture shown in Fig. 4c and calculate $P_\sigma(n) - P(n)$. The MCD's most significant effect on the switching probability is observed in the middle section of the figure, specifically for cells with n = 0 or n = 1 aligned neighbors, where the domain network's nanotexture is the most complex.

The outcome of this model is a detailed explanation of helicity and texture-dependent switching in ferromagnetic thin films at the nanoscale. Initially, a laser pulse with above-threshold fluence nucleates isolated domains stochastically. Following this, the growth of these domains occurs due to subsequent irradiation with laser pulses and nucleation of new domains and their coalescence with existing ones. The stochastic nature of this process leads to the formation of complex stochastic domain networks. When these stochastic domain networks are exposed to circularly polarized laser pulses, the switching probability is enhanced near complex magnetic nanotextures, leveling off the complexity of the existing domains and forming a deterministic switched state.

Conclusion

In summary, we used *in situ* MFM measurements to investigate how the domain nanotexture mediates multipulse helicity-dependent switching in a Pt/Co/Pt trilayer. Our results reveal that a single laser pulse stochastically nucleates sub-micrometer magnetic domains. Contrary to common belief, we find that the subsequent photo-induced growth of the domains is not driven by homogeneous growth due to an effective magnetic field, as previously conjectured for sub-micrometer magnetic domains. Instead, quantitative characterization of the emerging domain networks as a function of the number of laser pulses shows that the complexity of the domain network evolves distinct from the switched area. We introduced a novel measure for the switching efficiency based on the fractal dimensionality/complexity, which helped us to effectively track the evolution of the domain networks under irradiation of circularly polarized pulses. Our phenomenological modeling shows that the

switching probability depends not only on the helicity of light but also on the complexity of the domain nanotexture, providing qualitative agreement with the experimental results. Together, our experiments and modeling reveal that homogeneous and deterministic magnetization switching in the ferromagnetic Pt/Co/Pt system occurs via a laser-induced formation of domain networks —a helicity and texture-dependent effect. These findings open new pathways for leveraging inhomogeneous laser-induced heating to control ultrafast nanoscale magnetism, studying laser-induced complexity, and exploring photo-excitation effects in first-order phase transitions.

Methods

Sample fabrication. We engineered a multilayer structure with perpendicular magnetic anisotropy, composed of thin films of Ta (1.0 nm), MgO (2.0 nm), Pt (3.0 nm), Co (0.6 nm), Pt (3.0 nm), and Ta (4.0 nm) on a synthetic glass substrate. Using the Faraday rotation setup, we characterized the magnetic properties of the sample by measuring the out-of-plane hysteresis loop (see below). This structure exhibited a coercive field of approximately 28 mT, as shown in Extended Data Fig. 6. We chose to use a single Co layer based on the well-established finding that reducing the Co/Pt repeats leads to higher perpendicular magnetic anisotropy, larger domain size, and more efficient all-optical switching [37]. The symmetric structure was utilized to simplify the magnetic system and eliminate the Dzyaloshinsky-Moriya interaction [43].

Laser excitation. An amplified Ti:sapphire laser system (Spectra-Physics Spitfire Ace) with a central wavelength of 800 nm, controllable pulse width between 50 fs and 3ps, and a repetition rate of 1 kHz was used to control the sample surface's magnetization locally. We utilized 3 ps circularly polarized laser pulses with helicities defined as σ^+ and σ^- (for right and left-handed circularly polarized laser pulses, respectively). We used a quarter-wave plate to control the helicity of the laser pulses and an external Pockels cell to control the number of pulses during sequential illumination. The excitation beam used to obtain the data in Fig. 1 and 2, Extended Data Fig. 1, 2, 7, 8, and 9 is elliptical with a Gaussian profile, with a full width at half maximum of 35 μm and 107 μm for the x and y axes, respectively. The excitation beam used in Fig. 3, Ext. Data Fig. 3, and 5 is circular with a Gaussian profile and a beam diameter at full width at half maximum of approximately 60 μm.

Faraday rotation setup. We used the Faraday effect to measure the sample's hysteresis loop. As a source, we utilized a HeNe laser. For the polarizer and analyzer, we used Glan-Taylor polarizer. The laser light was modulated using a photoelastic modulator and focused on the sample positioned between the poles of an electromagnet with holes. The magnetic field was applied in an out-of-plane geometry. The laser passed through the poles and the sample and was collimated by a second lens, after which the beam went through an analyzer and was detected using a single diode and lock-in amplifier. The reference signal for the lock-in was taken from the photoelastic modulator controller.

Faraday microscopy setup. We used the magneto-optical Faraday effect to visualize the laser-induced domains in the Pt/Co/Pt trilayer. A monochromatic and coherent laser source (HeNe laser) illuminated the sample at a central wavelength of 633 nm. A beam expander was employed to enlarge the beam and uniformly illuminate the sample. We used Glan-Taylor polarizers as both polarizers and analyzers. To magnify the image, we utilized a 10x objective lens. After the analyzer, the light was projected onto the CCD camera (Coolsnap HQ). The laser excitation beam was aligned in a non-collinear geometry and focused on the sample surface with a 250 mm focal length lens.

Deterministic switching conditions. To establish the switching conditions, we utilized magneto-optical microscopy in a Faraday geometry. First, we identified the effect of the circularly polarized light pulses on the switching process using a swiping technique [29]. The result is shown in Extended Data Fig. 7. We observed that σ^- circularly polarized pulses deterministically switch the magnetization from the "up" state (M =1) to the "down" state (M =−1). Second, we varied the fluence and the number of σ^- pulses on different sample spots and monitored the final state of the Pt/Co/Pt exposed to laser pulses (see Extended Data Fig. 1a). We defined the condition as deterministically switched when the magnetization in the center of the spot was homogeneous, and there were no domain networks. The switching efficiency diagram can be found in Extended Data Fig. 1b. One can see that homogeneous switching from magnetization $M = 1$ to magnetization $M = -1$ could be achieved for fluences lower than ∼2.6 mJ/cm^2. The minimum number of pulses required for deterministic switching was 10, consistent with previous studies [30].

MFM. We utilized an NT-MDT NTEGRA Atomic Force Microscope for the MFM measurements. In our experiment, the scanning head of the microscope is coupled with the MFM tip. The scanning head can be removed, which completely separates the tip from the sample. Afterwards, the sample is exposed to the laser beam, and the scanning head is repositioned to approach the sample surface. MFM images were acquired with a probe height of

less than 100 nm. Two-pass MFM method was used. Low-moment MFM tips (NT-MDT MFM LM) were utilized to avoid disturbing the magnetic domains in Pt/Co/Pt. MFM images were corrected using the median line correction method. A direct comparison of the magneto-optical snapshots with the MFM maps shows a substantial spatial resolution enhancement (see Extended Data Fig. 8). Using MFM, it was possible to observe nanoscopic domains with sizes as small as ~200 nm (see Extended Data Fig. 9).

Single pulse helicity-dependent nucleation. We quantified the effect of the single laser pulse fluence and MCD effect on the nucleation of the nanoscale domains. To this end, we performed fluence dependence measurements of both (σ^-) and (σ^+) circular polarized pulses [31–35]. The result is shown in Extended Data Fig. 5a. We observed that the threshold for small domains is F_c^-=2.57 mJ/cm^2 for σ^- pulses, while for σ^+ pulses, the critical threshold fluence is F_c^+=2.7 mJ/cm^2. The difference between F_c^+ and F_c^- confirms that the absorption of σ^+ and σ^- pulses is inequivalent, which can be attributed to the MCD effect. In the present case, the wavelength of the laser is 800 nm, for which the typical value of the MCD in Pt/Co/Pt is approximately 1.5% [53]. In Extended Data Fig. 5b, we plot A_s/A_b as a function of helicity and fluence and extract an MCD-induced shift in the fluence dependence of approximately 3%. Extended Data Fig. 5c shows that the fractal dimension D also exhibits an MCD effect but with a slightly smaller shift of approximately 1.5%. We observe that both A_s/A_b and D exhibit nonlinear growth as a function of fluence. Interestingly, D increases and saturates at approximately 1.4 for a 2.9 mJ/cm^2 fluence.

Simulations. Simulations were conducted using a square grid of 100x50 cells model system. Each cell interacts with its neighbors, and the energy required to switch these domains depends on the nearest-neighbor alignments. We utilized Equation (1) to estimate the energy barriers using E_0 and E_1, which are extracted from the micromagnetic model (details are provided in Supplementary Note 2). The laser pulse is modeled as a temperature profile in time. For simplicity, the temperature $T(t)$ follows an exponential rise and decay defined by dT/dt, during the laser pulse

$$\frac{dT}{dt} = \begin{cases} (T - T_\mathrm{p})/\tau_{rise}\,, & \text{during pulse} \\ (T - T_0)/\tau_{fall}\,, & \text{otherwise} \end{cases}. \tag{3}$$

For the duration $w_{\mathrm{pulse}} = 30\tau_0$ of the laser pulses, the temperature goes to a peak T_p on a timescale $\tau_{\mathrm{rise}} = \tau_0$ (for simplicity, the heating is almost instant) and to a base temperature $T_0 = 0.2E_0/k_\mathrm{B}$ on a timescale $\tau_{fall} = 30\tau_0$ otherwise. We found that this pulse duration in our simulation qualitatively reproduces single-pulse domain nucleation with 3 ps pulses (See Supplementary Note 3).

The peak temperature during the laser pulse is influenced by both the position and the direction of the local magnetization. This is because the laser has a Gaussian profile in space, and the heating of the cells is affected by their magnetization M through the MCD effect. This leads to

$$T_p = T_p(M, \mathrm{r}) = T_0 + (1 - \alpha M)T_{peak} exp\left(\frac{\mathbf{r}-\mathbf{r}_0}{2\sigma_p}\right), \tag{4}$$

where $\alpha = 0.025$ is the MCD factor, leading to a 4% difference in heating, r_0 is the position of the laser, $\sigma_\mathrm{p} = 8\mu$m (40 cells) is the width of the Gaussian profile, $T_{\mathrm{peak}} = E_0/k_\mathrm{B}$. The time interval between laser pulses was $300\tau_0$.

Calculating the fractal dimension directly from the simulation images poses a challenge due to the low resolution, where the relevant shapes are approximately of the same size as the pixels. To effectively compare the simulations with the MFM images, we refined the mesh by a factor of 10 and applied a Gaussian filter with a standard deviation of σ = 100 nm to simulate the resolution of MFM. In the box-counting method for calculating the fractal dimension, we only consider the points corresponding to the largest six box sizes for the fit (See Extended Data Fig. 4). The simulated switched area and fractal dimension data shown in Fig. 2b are the average and standard error over 50 runs for improved accuracy and to account for the stochastic nature of the model.

Data availability

Source data for the figures are publicly available at https://doi.org/10.34973/6j6t-pd76. All other data that support the findings of this paper are available from the corresponding authors upon request.

Acknowledgments

The authors thank N. Kiselev, D. Grundler, R. Medapalli, and L. Körber for fruitful discussions, and K. Saeedi and C. Berkhout for their technical support. Additionally, the authors would like to thank N. Khokhlov, V. Bilyk, L. Nowak, and J. Hintermayr, for their assistance with the building of the experimental setup. This work was funded by ERC grant 485 101078206 ASTRAL, the European Union Horizon 2020 and innovation program under the European Research Council ERC Grant Agreement No. 856538 (3D-MAGiC), the European Union Horizon 2020 innovation program under the Marie Skłodowska-Curie Grant Agreement No. 861300 (COMRAD), the Gravitation program of the Dutch Ministry of Education, Culture and Science (OCW) under the research program "Materials for the Quantum Age" (QuMat) registration number 024.005.006. F. Kammerbauer and M. Kläui acknowledge funding by the Deutsche Forschungsgemeinschaft (DFG, German Research Foundation) TRR 173/2 Spin+X (Project A01, A12, and B02). M. Na acknowledges the support of the Natural Sciences and Engineering Research Council of Canada (NSERC) PDF fellowship. R. Mikhaylovskiy acknowledges support from European Research Council ERC Grant Agreement No. 852050 (MAGSHAKE). J. H. Mentink acknowledges funding from the VIDI project no. 223.157 (CHASEMAG). J. H. Mentink and M. Kläui acknowledge the Horizon Europe Framework Program of the European Commission under project no. 101070290 (NIMFEIA) and with Th. Rasing also by the KIC project no. 22016, which are (partly) financed by the Dutch Research Council (NWO).
.

Author contributions

D. A., J. H. M., A. K., and T. R. conceived the project. D. A., J. H. M., A. K., and T. R. supervised the study. D. Kh. and D. K. designed and built the experimental setup. D. Kh. and, N. V. performed the experiments. F. K., R. F., and M. K. fabricated the samples. D. Kh. analyzed and interpreted the results of MFM and magneto-optical experiments. D. Kh. and M. N. prepared figures. R. L. and J. H. M. provided the theoretical model. R. L. carried out the simulations. D. Kh., R. L., M. N., R. M., J. H. M., D. A., A. K., and T. R. wrote the original draft with feedback from all the co-authors.

Competing interests

The authors declare no competing interests.

References

1. Collet, E., Lemée-Cailleau, M.-H., Buron-Le Cointe, M., Cailleau, H., Wulff, M., Luty, T., Koshihara, S.-Y., Meyer, M., Toupet, L., Rabiller, P., Techert, S.: Laser-Induced Ferroelectric Structural Order in an Organic Charge-Transfer Crystal. Science. 300, 612–615 (2003). https://doi.org/10.1126/science.1082001

2. Beaud, P., Caviezel, A., Mariager, S.O., Rettig, L., Ingold, G., Dornes, C., Huang, S.-W., Johnson, J.A., Radovic, M., Huber, T., Kubacka, T., Ferrer, A., Lemke, H.T., Chollet, M., Zhu, D., Glownia, J.M., Sikorski, M., Robert, A., Wadati, H., Nakamura, M., Kawasaki, M., Tokura, Y., Johnson, S.L., Staub, U.: A time-dependent order parameter for ultrafast photoinduced phase transitions. Nature Materials. 13, 923–927 (2014). https://doi.org/10.1038/nmat4046

3. Wall, S., Yang, S., Vidas, L., Chollet, M., Glownia, J.M., Kozina, M., Katayama, T., Henighan, T., Jiang, M., Miller, T.A., Reis, D.A., Boatner, L.A., Delaire, O., Trigo, M.: Ultrafast disordering of vanadium dimers in photoexcited VO 2. Science. 362, 572–576 (2018). https://doi.org/10.1126/science.aau3873

4. Stoica, V.A., Yang, T., Das, S., Cao, Y., Wang, H., Kubota, Y., Dai, C., Padma, H., Sato, Y., Mangu, A., Nguyen, Q.L., Zhang, Z., Talreja, D., Zajac, M.E., Walko, D.A., DiChiara, A.D., Owada, S., Miyanishi, K., Tamasaku, K., Sato, T., Glownia, J.M., Esposito, V., Nelson, S., Hoffmann, M.C., Schaller, R.D., Lindenberg, A.M., Martin, L.W., Ramesh, R., Matsuda, I., Zhu, D., Chen, L.-Q., Wen, H., Gopalan, V., Freeland, J.W.:

Non-equilibrium pathways to emergent polar supertextures. Nature Materials. (2024). https://doi.org/10.1038/s41563-024-01981-2

5. Nova, T.F., Disa, A.S., Fechner, M., Cavalleri, A.: Metastable ferroelectricity in optically strained SrTiO 3. Science. 364, 1075–1079 (2019). https://doi.org/10.1126/science.aaw4911

6. Li, X., Qiu, T., Zhang, J., Baldini, E., Lu, J., Rappe, A.M., Nelson, K.A.: Terahertz field–induced ferroelectricity in quantum paraelectric SrTiO3. Science. 364, 1079–1082 (2019). https://doi.org/10.1126/science.aaw4913

7. Gedik, N., Yang, D.-S., Logvenov, G., Bozovic, I., H., Zewail.A.: Nonequilibrium Phase Transitions in Electron Crystallography. Science. 316, 425–429 (2007)

8. Demsar, J., Podobnik, B., Kabanov, V.V., Wolf, Th., Mihailovic, D.: Superconducting Gap Dc, the Pseudogap Dp, and Pair Fluctuations above Tc in Overdoped Y1-xCaxBa2Cu3O72-d from Femtosecond Time-Domain Spectroscopy. Physical Review Letters. 82, 4918–4921 (1999). https://doi.org/10.1103/PhysRevLett.82.4918

9. Boschini, F., da Silva Neto, E.H., Razzoli, E., Zonno, M., Peli, S., Day, R.P., Michiardi, M., Schneider, M., Zwartsenberg, B., Nigge, P., Zhong, R.D., Schneeloch, J., Gu, G.D., Zhdanovich, S., Mills, A.K., Levy, G., Jones, D.J., Giannetti, C., Damascelli, A.: Collapse of superconductivity in cuprates via ultrafast quenching of phase coherence. Nature Materials. 17, 416–420 (2018). https://doi.org/10.1038/s41563-018-0045-1

10. Wandel, S., Boschini, F., da Silva Neto, E.H., Shen, L., Na, M.X., Zohar, S., Wang, Y., Welch, S.B., Seaberg, M.H., Koralek, J.D., Dakovski, G.L., Hettel, W., Lin, M.-F., Moeller, S.P., Schlotter, W.F., Reid, A.H., Minitti, M.P., Boyle, T., He, F., Sutarto, R., Liang, R., Bonn, D., Hardy, W., Kaindl, R.A., Hawthorn, D.G., Lee, J.-S., Kemper, A.F., Damascelli, A., Giannetti, C., Turner, J.J., Coslovich, G.: Enhanced charge density wave coherence in a light-quenched, high-temperature superconductor. Science. 376, 860–864 (2022). https://doi.org/10.1126/science.abd7213

11. Fava, S., De Vecchi, G., Jotzu, G., Buzzi, M., Gebert, T., Liu, Y., Keimer, B., Cavalleri, A.: Magnetic field expulsion in optically driven YBa2Cu3O6.48. Nature. (2024). https://doi.org/10.1038/s41586-024-07635-2

12. Beaurepaire, E., Merle, J.-C., Daunois, A., Bigot, J.-Y.: Ultrafast Spin Dynamics in Ferromagnetic Nickel. Physical Review Letters. 76, 4250–4253 (1996). https://doi.org/10.1103/PhysRevLett.76.4250

13. Radu, I., Vahaplar, K., Stamm, C., Kachel, T., Pontius, N., Dürr, H.A., Ostler, T.A., Barker, J., Evans, R.F.L., Chantrell, R.W., Tsukamoto, A., Itoh, A., Kirilyuk, A., Rasing, Th., Kimel, A.V.: Transient ferromagnetic-like state mediating ultrafast reversal of antiferromagnetically coupled spins. Nature. 472, 205–208 (2011). https://doi.org/10.1038/nature09901

14. Büttner, F., Pfau, B., Böttcher, M., Schneider, M., Mercurio, G., Günther, C.M., Hessing, P., Klose, C., Wittmann, A., Gerlinger, K., Kern, L.-M., Strüber, C., von Korff Schmising, C., Fuchs, J., Engel, D., Churikova, A., Huang, S., Suzuki, D., Lemesh, I., Huang, M., Caretta, L., Weder, D., Gaida, J.H., Möller, M., Harvey, T.R., Zayko, S., Bagschik, K., Carley, R., Mercadier, L., Schlappa, J., Yaroslavtsev, A., Le Guyarder, L., Gerasimova, N., Scherz, A., Deiter, C., Gort, R., Hickin, D., Zhu, J., Turcato, M., Lomidze, D., Erdinger, F., Castoldi, A., Maffessanti, S., Porro, M., Samartsev, A., Sinova, J., Ropers, C., Mentink, J.H., Dupé, B., Beach, G.S.D., Eisebitt, S.: Observation of fluctuation-mediated picosecond nucleation of a topological phase. Nature Materials. 20, 30–37 (2021). https://doi.org/10.1038/s41563-020-00807-1

15. Kirilyuk, A., Kimel, A.V., Rasing, T.: Ultrafast optical manipulation of magnetic order. Reviews of Modern Physics. 82, 2731–2784 (2010). https://doi.org/10.1103/RevModPhys.82.2731

16. Li, G., Medapalli, R., Mentink, J.H., Mikhaylovskiy, R.V., Blank, T.G.H., Patel, S.K.K., Zvezdin, A.K., Rasing, Th., Fullerton, E.E., Kimel, A.V.: Ultrafast kinetics of the antiferromagnetic-ferromagnetic phase transition in FeRh. Nature Communications. 13, 2998 (2022). https://doi.org/10.1038/s41467-022-30591-2

17. Blank, T.G.H., Grishunin, K.A., Ivanov, B.A., Mashkovich, E.A., Afanasiev, D., Kimel, A.V.: Empowering Control of Antiferromagnets by THz-Induced Spin Coherence. Physical Review Letters. 131, 096701 (2023). https://doi.org/10.1103/PhysRevLett.131.096701

18. Afanasiev, D., Hortensius, J.R., Ivanov, B.A., Sasani, A., Bousquet, E., Blanter, Y.M., Mikhaylovskiy, R.V., Kimel, A.V., Caviglia, A.D.: Ultrafast control of magnetic interactions via light-driven phonons. Nature Materials. 20, 607–611 (2021). https://doi.org/10.1038/s41563-021-00922-7

19. Davies, C.S., Prabhakara, K.H., Davydova, M.D., Zvezdin, K.A., Shapaeva, T.B., Wang, S., Zvezdin, A.K., Kirilyuk, A., Rasing, Th., Kimel, A.V.: Anomalously Damped Heat-Assisted Route for Precessional Magnetization Reversal in an Iron Garnet. Physical Review Letters. 122, 027202 (2019). https://doi.org/10.1103/PhysRevLett.122.027202

20. Liu, M., Hwang, H.Y., Tao, H., Strikwerda, A.C., Fan, K., Keiser, G.R., Sternbach, A.J., West, K.G., Kittiwatanakul, S., Lu, J., Wolf, S.A., Omenetto, F.G., Zhang, X., Nelson, K.A., Averitt, R.D.: Terahertz-field-induced insulator-to-metal transition in vanadium dioxide metamaterial. Nature. 1–4 (2012). https://doi.org/10.1038/nature11231

21. de Jong, S., Kukreja, R., Trabant, C., Pontius, N., Chang, C.F., Kachel, T., Beye, M., Sorgenfrei, F., Back, C.H., Bräuer, B., Schlotter, W.F., Turner, J.J., Krupin, O., Doehler, M., Zhu, D., Hossain, M.A., Scherz, A.O., Fausti, D., Novelli, F., Esposito, M., Lee, W.S., Chuang, Y.D., Lu, D.H., Moore, R.G., Yi, M., Trigo, M., Kirchmann, P., Pathey, L., Golden, M.S., Buchholz, M., Metcalf, P., Parmigiani, F., Wurth, W., Föhlisch, A., Schüßler-Langeheine, C., Dürr, H.A.: Speed limit of the insulator–metal transition in magnetite. Nature Materials. 12, 882–886 (2013). https://doi.org/10.1038/nmat3718

22. Mankowsky, R., Von Hoegen, A., Först, M., Cavalleri, A.: Ultrafast Reversal of the Ferroelectric Polarization. Physical Review Letters. 118, 197601 (2017). https://doi.org/10.1103/PhysRevLett.118.197601

23. Stojchevska, L., Vaskivskyi, I., Mertelj, T., Kusar, P., Svetin, D., Brazovskii, S., Mihailovic, D.: Ultrafast Switching to a Stable Hidden Quantum State in an Electronic Crystal. Science. 344, 177–180 (2014). https://doi.org/10.1126/science.1241591

24. Ravnik, J., Diego, M., Gerasimenko, Y., Vaskivskyi, Y., Vaskivskyi, I., Mertelj, T., Vodeb, J., Mihailovic, D.: A time-domain phase diagram of metastable states in a charge ordered quantum material. Nature Communications. 12, 2323 (2021). https://doi.org/10.1038/s41467-021-22646-7

25. Johnson, A.S., Pastor, E., Batlle-Porro, S., Benzidi, H., Katayama, T., de la Peña Muñoz, G.A., Krapivin, V., Kim, S., López, N., Trigo, M., Wall, S.E.: All-optical seeding of a light-induced phase transition with correlated disorder. Nature Physics. 20, 970–975 (2024). https://doi.org/10.1038/s41567-024-02474-4

26. Kimel, A.V., Kirilyuk, A., Usachev, P.A., Pisarev, R.V., Balbashov, A.M., Rasing, Th.: Ultrafast non-thermal control of magnetization by instantaneous photomagnetic pulses. Nature. 435, 655–657 (2005). https://doi.org/10.1038/nature03564

27. Hansteen, F., Kimel, A., Kirilyuk, A., Rasing, T.: Femtosecond Photomagnetic Switching of Spins in Ferrimagnetic Garnet Films. Physical Review Letters. 95, 047402 (2005). https://doi.org/10.1103/PhysRevLett.95.047402

28. de Jong, J.A., Razdolski, I., Kalashnikova, A.M., Pisarev, R.V., Balbashov, A.M., Kirilyuk, A., Rasing, Th., Kimel, A.V.: Coherent Control of the Route of an Ultrafast Magnetic Phase Transition via Low-Amplitude Spin Precession. Physical Review Letters. 108, 157601 (2012). https://doi.org/10.1103/PhysRevLett.108.157601

29. Lambert, C.-H., Mangin, S., Varaprasad, B.S.D.Ch.S., Takahashi, Y.K., Hehn, M., Cinchetti, M., Malinowski, G., Hono, K., Fainman, Y., Aeschlimann, M., Fullerton, E.E.: All-optical control of ferromagnetic thin films and nanostructures. Science. 345, 1337–1340 (2014). https://doi.org/10.1126/science.1253493

30. Kichin, G., Hehn, M., Gorchon, J., Malinowski, G., Hohlfeld, J., Mangin, S.: From Multiple- to Single-Pulse All-Optical Helicity-Dependent Switching in Ferromagnetic Co/Pt Multilayers. Physical Review Applied. 12, 024019 (2019). https://doi.org/10.1103/PhysRevApplied.12.024019

31. Gorchon, J., Yang, Y., Bokor, J.: Model for multishot all-thermal all-optical switching in ferromagnets. Physical Review B. 94, 020409 (2016). https://doi.org/10.1103/PhysRevB.94.020409

32. Ellis, M.O.A., Fullerton, E.E., Chantrell, R.W.: All-optical switching in granular ferromagnets caused by magnetic circular dichroism. Scientific Reports. 6, 30522 (2016). https://doi.org/10.1038/srep30522

33. Medapalli, R., Afanasiev, D., Kim, D.K., Quessab, Y., Manna, S., Montoya, S.A., Kirilyuk, A., Rasing, Th., Kimel, A.V., Fullerton, E.E.: Multiscale dynamics of helicity-dependent all-optical magnetization reversal in ferromagnetic Co/Pt multilayers. Physical Review B. 96, 224421 (2017). https://doi.org/10.1103/PhysRevB.96.224421

34. Quessab, Y., Medapalli, R., El Hadri, M.S., Hehn, M., Malinowski, G., Fullerton, E.E., Mangin, S.: Helicity-dependent all-optical domain wall motion in ferromagnetic thin films. Physical Review B. 97, 054419 (2018). https://doi.org/10.1103/PhysRevB.97.054419

35. Yamada, K.T., Kimel, A.V., Prabhakara, K.H., Ruta, S., Li, T., Ando, F., Semin, S., Ono, T., Kirilyuk, A., Rasing, T.: Efficient All-Optical Helicity Dependent Switching of Spins in a Pt/Co/Pt Film by a Dual-Pulse Excitation. Frontiers in Nanotechnology. 4, (2022). https://doi.org/10.3389/fnano.2022.765848

36. Janda, T., Roy, P.E., Otxoa, R.M., Šobáň, Z., Ramsay, A., Irvine, A.C., Trojanek, F., Surýnek, M., Campion, R.P., Gallagher, B.L., Němec, P., Jungwirth, T., Wunderlich, J.: Inertial displacement of a domain wall excited by ultra-short circularly polarized laser pulses. Nat Commun. 8, 15226 (2017). https://doi.org/10.1038/ncomms15226

37. Parlak, U., Adam, R., Bürgler, D.E., Gang, S., Schneider, C.M.: Optically induced magnetization reversal in [Co/Pt] multilayers: Role of domain wall dynamics. Physical Review B. 98, 214443 (2018). https://doi.org/10.1103/PhysRevB.98.214443

38. Je, S.-G., Vallobra, P., Srivastava, T., Rojas-Sánchez, J.-C., Pham, T.H., Hehn, M., Malinowski, G., Baraduc, C., Auffret, S., Gaudin, G., Mangin, S., Béa, H., Boulle, O.: Creation of Magnetic Skyrmion Bubble Lattices by Ultrafast Laser in Ultrathin Films. Nano Letters. 18, 7362–7371 (2018). https://doi.org/10.1021/acs.nanolett.8b03653

39. Kazakova, O., Puttock, R., Barton, C., Corte-León, H., Jaafar, M., Neu, V., Asenjo, A.: Frontiers of magnetic force microscopy. Journal of Applied Physics. 125, (2019). https://doi.org/10.1063/1.5050712

40. Schwarz, A., Wiesendanger, R.: Magnetic sensitive force microscopy. Nano Today. 3, 28–39 (2008). https://doi.org/10.1016/S1748-0132(08)70013-6

41. Huo, S., Bishop, J.E.L., Tucker, J.W., Al-Khafaji, M.A., Rainforth, W.M., Davies, H.A., Gibbs, M.R.J.: Micromagnetic and MFM studies of a domain wall in thick 110 FeSi. Journal of Magnetism and Magnetic Materials. 190, 17–27 (1998). https://doi.org/10.1016/S0304-8853(98)00279-0

42. Okuno, T., Shigeto, K., Ono, T., Mibu, K., Shinjo, T.: MFM study of magnetic vortex cores in circular permalloy dots: behavior in external field. Journal of Magnetism and Magnetic Materials. 240, 1–6 (2002). https://doi.org/10.1016/S0304-8853(01)00708-9

43. Hrabec, A., Porter, N.A., Wells, A., Benitez, M.J., Burnell, G., McVitie, S., McGrouther, D., Moore, T.A., Marrows, C.H.: Measuring and tailoring the Dzyaloshinskii-Moriya interaction in perpendicularly magnetized thin films. Physical Review B. 90, 020402 (2014). https://doi.org/10.1103/PhysRevB.90.020402

44. Casiraghi, A., Corte-León, H., Vafaee, M., Garcia-Sanchez, F., Durin, G., Pasquale, M., Jakob, G., Kläui, M., Kazakova, O.: Individual skyrmion manipulation by local magnetic field gradients. Communications Physics. 2, 145 (2019). https://doi.org/10.1038/s42005-019-0242-5

45. Bhukta, M., Dohi, T., Bharadwaj, V.K., Zarzuela, R., Syskaki, M.-A., Foerster, M., Niño, M.A., Sinova, J., Frömter, R., Kläui, M.: Homochiral antiferromagnetic merons, antimerons and bimerons realized in synthetic antiferromagnets. Nature Communications. 15, 1641 (2024). https://doi.org/10.1038/s41467-024-45375-z

46. Peng, Y., Salomoni, D., Malinowski, G., Zhang, W., Hohlfeld, J., Buda-Prejbeanu, L.D., Gorchon, J., Vergès, M., Lin, J.X., Lacour, D., Sousa, R.C., Prejbeanu, I.L., Mangin, S., Hehn, M.: In-plane reorientation induced single laser pulse magnetization reversal. Nature Communications. 14, 5000 (2023). https://doi.org/10.1038/s41467-023-40721-z

47. Berritta, M., Mondal, R., Carva, K., Oppeneer, P.M.: Ab InitioTheory of Coherent Laser-Induced Magnetization in Metals. Physical Review Letters. 117, 137203 (2016). https://doi.org/10.1103/PhysRevLett.117.137203

48. John, R., Berritta, M., Hinzke, D., Müller, C., Santos, T., Ulrichs, H., Nieves, P., Walowski, J., Mondal, R., Chubykalo-Fesenko, O., McCord, J., Oppeneer, P.M., Nowak, U., Münzenberg, M.: Magnetisation switching of FePt nanoparticle recording medium by femtosecond laser pulses. Scientific Reports. 7, 4114 (2017). https://doi.org/10.1038/s41598-017-04167-w

49. El Hadri, M.S., Pirro, P., Lambert, C.-H., Petit-Watelot, S., Quessab, Y., Hehn, M., Montaigne, F., Malinowski, G., Mangin, S.: Two types of all-optical magnetization switching mechanisms using femtosecond laser pulses. Physical Review B. 94, 064412 (2016). https://doi.org/10.1103/PhysRevB.94.064412

50. Lisovskii, F.V., Lukashenko, L.I., Mansvetova, E.G.: Thermodynamically stable fractal-like domain structures in magnetic films. Journal of Experimental and Theoretical Physics Letters. 79, 352–354 (2004). https://doi.org/10.1134/1.1765181

51. Pylypovskyi, O.V., Hedrich, N., Tomilo, A.V., Kosub, T., Wagner, K., Hübner, R., Shields, B., Sheka, D.D., Fassbender, J., Maletinsky, P., Makarov, D.: Interaction of Domain Walls with Grain Boundaries in Uniaxial Insulating Antiferromagnets. Physical Review Applied. 20, 014020 (2023). https://doi.org/10.1103/PhysRevApplied.20.014020

52. Möhrke, P., Rhensius, J., Thiele, J.-U., Heyderman, L.J., Kläui, M.: Tailoring laser-induced domain wall pinning. Solid State Communications. 150, 489–491 (2010). https://doi.org/10.1016/j.ssc.2009.11.040

53. Yamada, K.T., Davies, C.S., Ando, F., Li, T., Ono, T., Rasing, T., Kimel, A.V., Kirilyuk, A.: Magnetization reversal of a ferromagnetic Pt/Co/Pt film by helicity dependent absorption of visible to near-infrared laser pulses. Phys. Rev. B. 111, L020406 (2025). https://doi.org/10.1103/PhysRevB.111.L020406

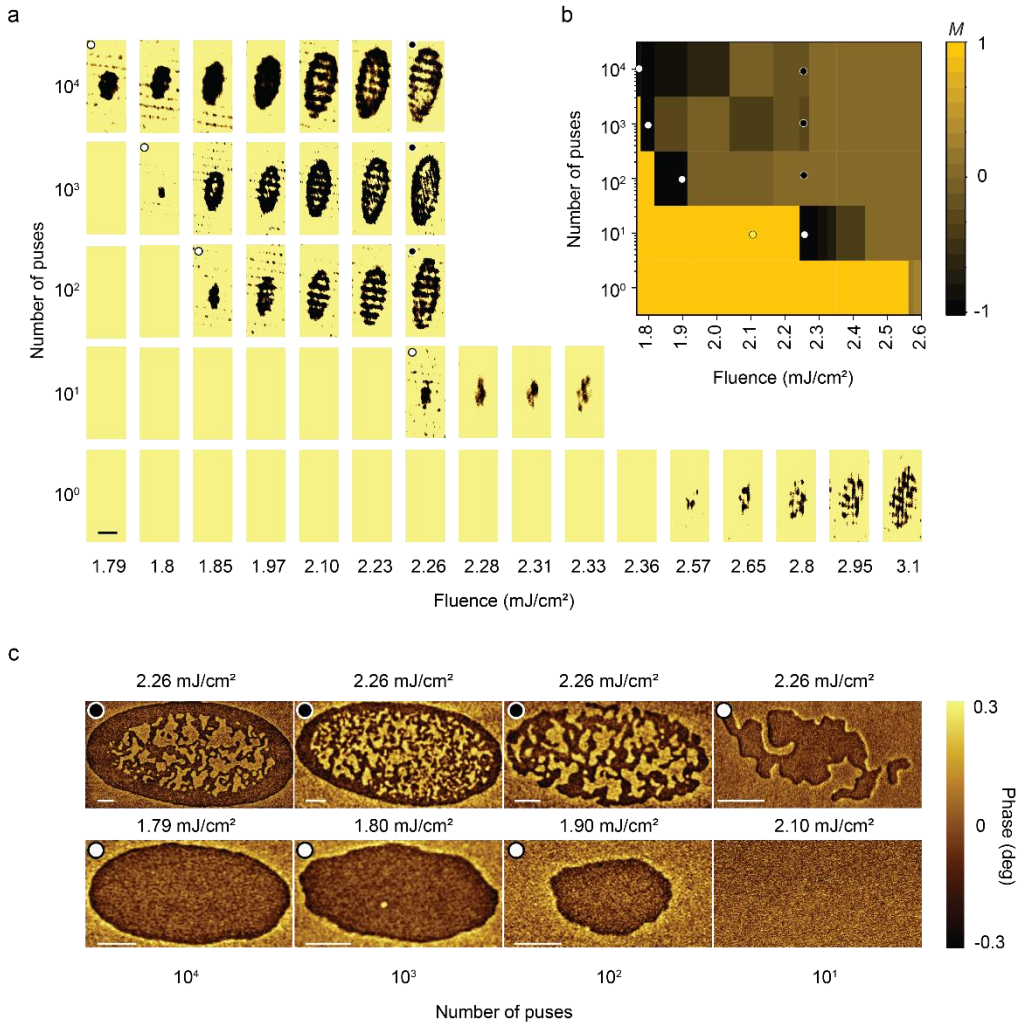

Extended Data Fig. 1 Conditions for deterministic switching in Pt/Co/Pt. (a) Magneto-optical images of the magnetization after illumination with σ laser pulses as a function of the number of pulses and fluence. Magneto-optical images were obtained using magneto-optical Faraday microscopy. Images were post-processed by removing the background. The images of the ground state, unaffected by laser pulses, are replaced by a uniform yellow background. The scale bar is 15 µm. **(b)** Diagram of the average magnetization after laser illumination inside the switched spot as a function of the number of pulses and fluence. Dots in the corners of the images represent the MFM sampled images in deterministic (white) and mixed states (black) displayed in **(c).** The scale bars in **(c)** are 5 µm.

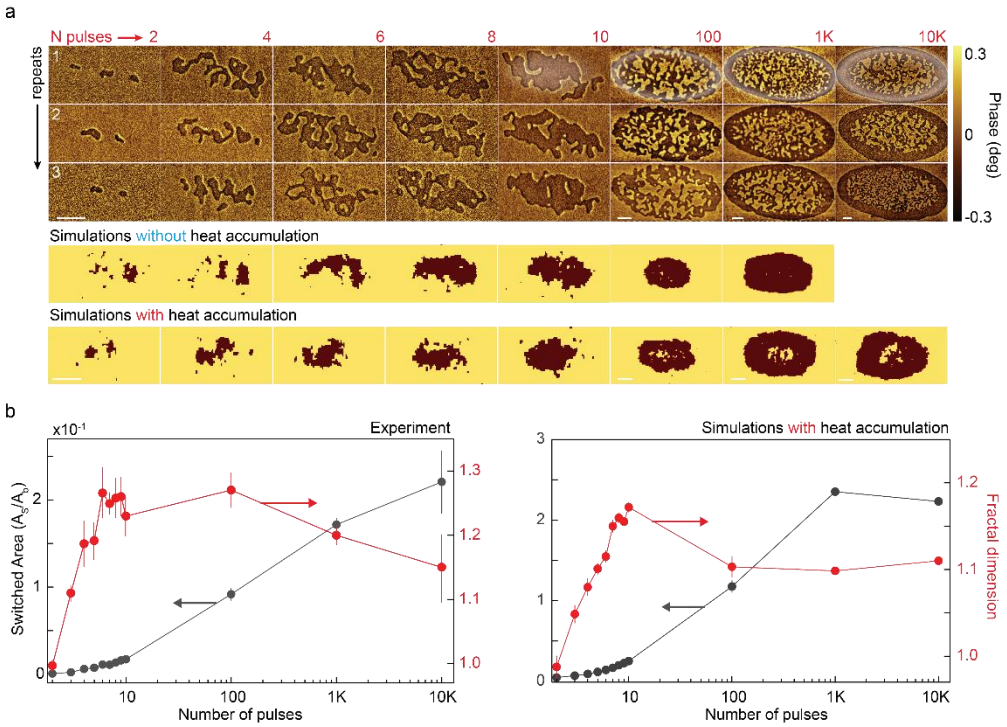

Extended Data Fig. 2 Complete multi-pulse evolution of helicity-dependent switching up to 10 thousand pulses. **(a)** MFM images of the laser-induced stochastic domain networks as a function of the number of pulses N at a fluence of $F = 2.26$ mJ/cm^2. The white shadow indicates progress in the deterministic state formation. The lower panel shows the result of the simulations using a probabilistic energy barrier-based model, including and excluding heat accumulation. We see that heat accumulation doesn't affect the formation of the homogeneously switched domain at a low number of pulses. Heat accumulation was implemented in the model as an exponential growth of the base temperature from $T_0 = 0.2E_0/k_B$ to $T_0 = 0.5E_0/k_B$ saturating at ~100 pulses. The scale bars are 5 µm. **(b)** The normalized switched area A_s/A_b (gray) and the fractal dimension D (red) as a function of the incident number of circularly polarized laser pulses N, calculated from the experiment and simulations, respectively. We run the simulation 50 times from 0 to 10 pulses, 3 times in the range 100 to 1000 pulses, and 1 time for 10000 pulses. We use only the outer domain wall to estimate the fractal dimension of the deterministic part in the mixed state. The switched area increases linearly up to 10 pulses and then saturates after 100 pulses, followed by a slow growth, as observed in the experiment and simulation. In D, we observe a rapid increase to D ~ 1.24 (1.17) from 0 to 6(7) pulses, followed by a plateau from 6(7) to 100(10), and a decrease to D ~ 1.15 (1.11) from 100(10) to 10K pulses for experiments (simulations).

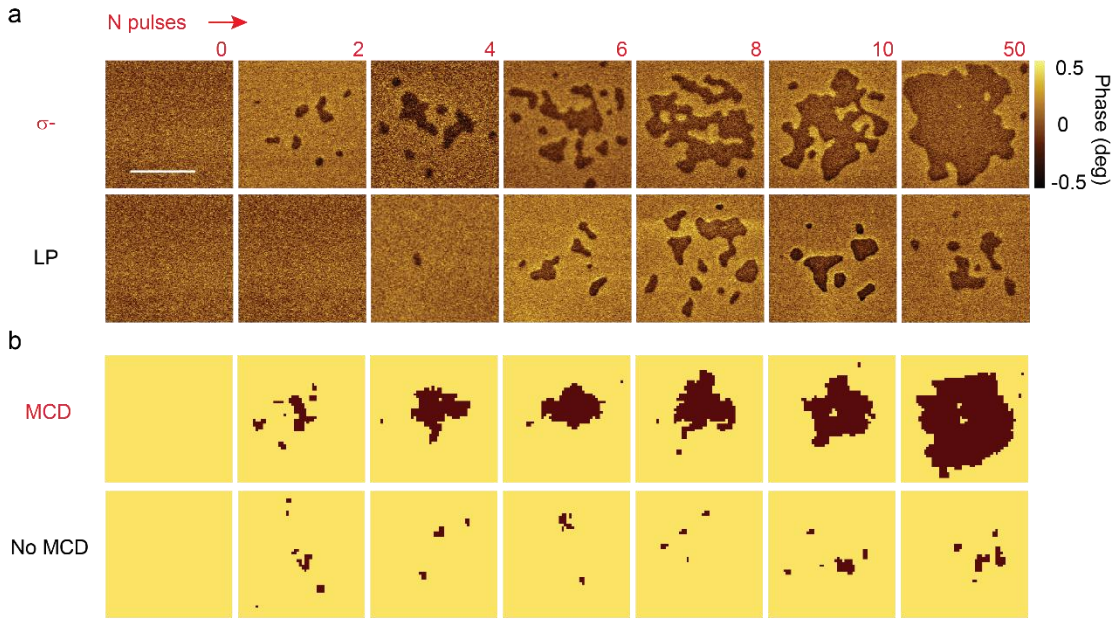

Extended Data Fig. 3 Effect of MCD on laser-induced evolution of stochastic domain networks. **(a)** MFM images of the laser-induced nanosized domain networks as a function of the number of σ^- and LP pulses. Fluence was fixed at a value of about 2.5 mJ/cm^2**. (b)** Simulated images of the laser-induced domains with and without the contribution of the MCD effect. The scale bar is 5 μm.

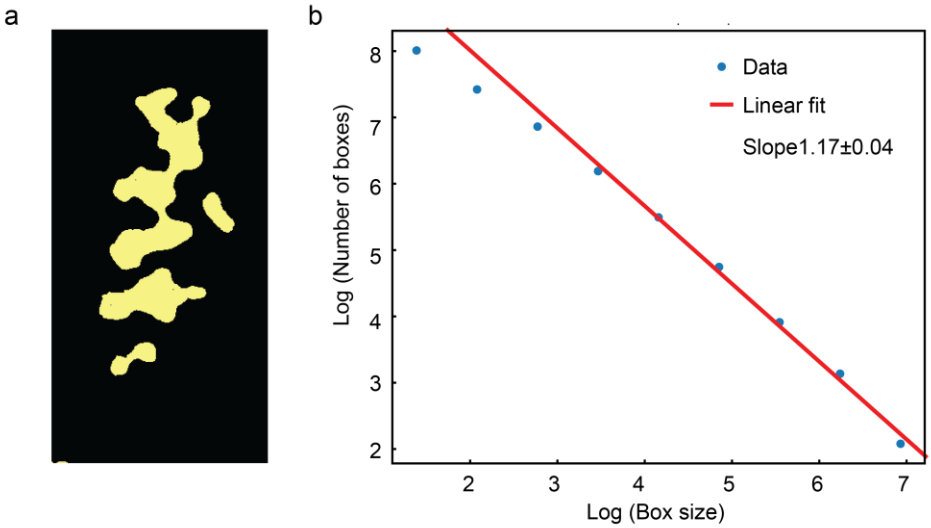

Extended Data Fig. 4 An example of the fractal dimension calculation using the Minkovski-Bouligand method. (a) Binary MFM image of the sample after illumination with 4 pulses. **(b)** Graph of the logarithm of box size plotted against the logarithm of box number with a linear fit showing a value for D = 1.17±0.04.

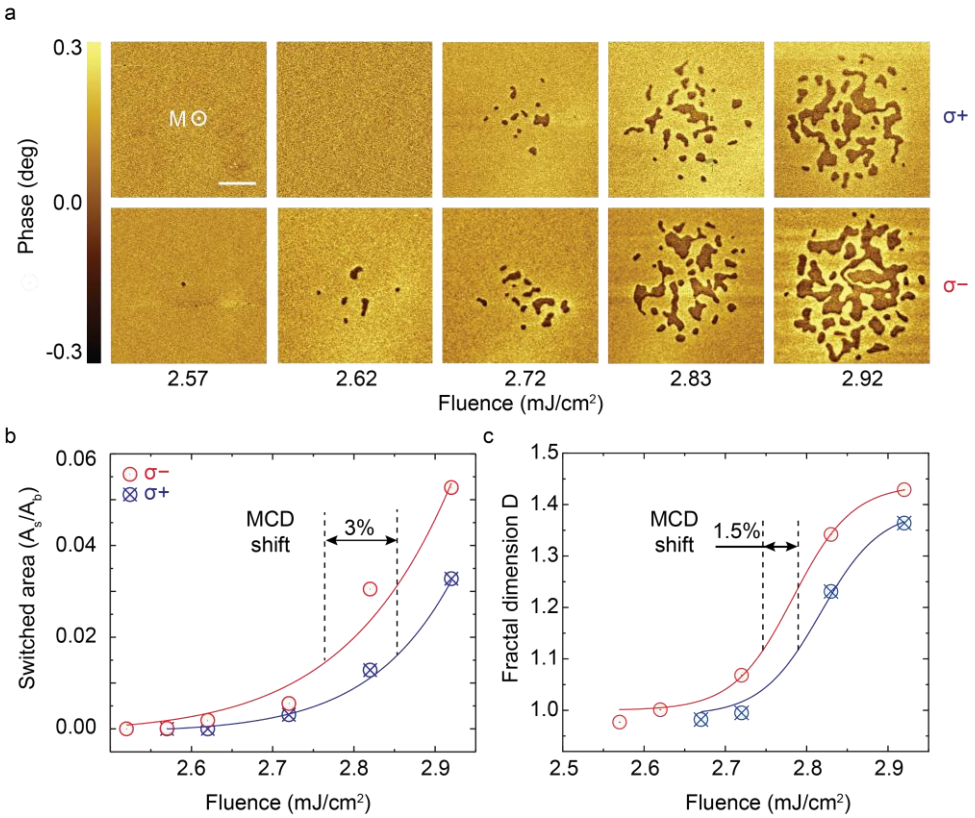

Extended Data Fig. 5 Single-pulse nucleation of the domain networks. (a) MFM images of the single-pulse nucleated domains as a function of pulse fluence for left (σ^-) and right (σ^+) circularly polarized laser pulses. We observe that the threshold for small domains is F_{σ^-}=2.57 mJ/cm^2 for σ^- pulses, while for σ^+ pulses, the critical threshold fluence is F_{σ^+}=2.7 mJ/cm^2. The difference between F_{σ^+} and F_{σ^-} confirms that the absorption of σ^+ and σ^- pulses is inequivalent, which can be attributed to the MCD effect. The scale bar is 5 μm**. (b-c)** Switched area **(b)** and fractal dimension **(c)** as a function of fluence for the domain networks**.** Extracted an MCD-induced shift in A_s/A_b as the function of fluence is approximately 3%. Fractal dimension D also exhibits an MCD effect but with a slightly smaller induced shift of approximately 1.5%. Solid lines in (b,c) serve as a guide for the eye.

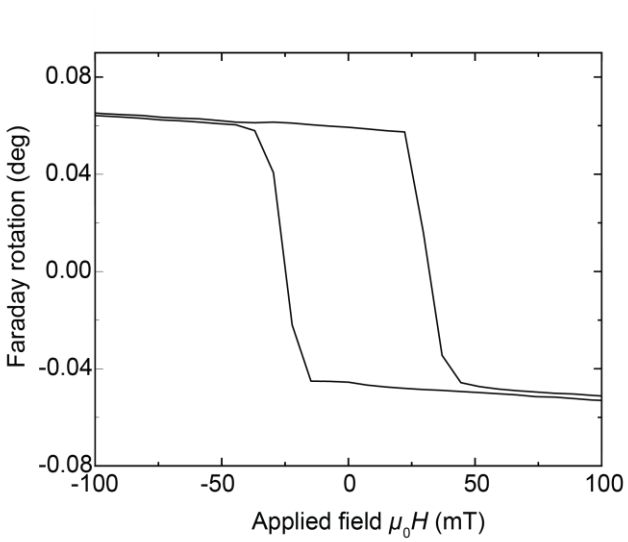

Extended Data Fig. 6 Magnetic hysteresis loop for Pt(3 nm)/Co(0.6 nm)/Pt(3 nm). The hysteresis loop is measured by observing the Faraday rotation in response to changes in an applied magnetic field.

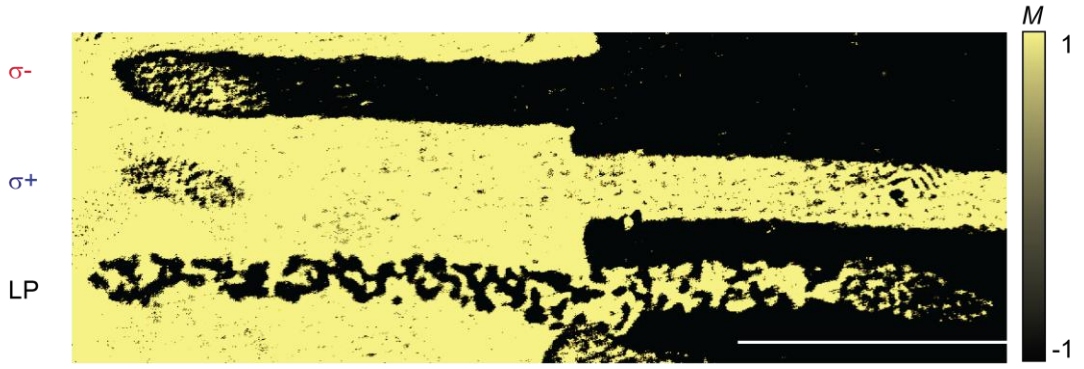

Extended Data Fig. 7 Effect of the light helicity on the switching. Magneto-optical image of two domains with M=1 and M=−1 after sweeping with a laser beam with $\sigma-$, $\sigma+$, and linearly polarized light (LP). Image shows that to switch magnetization from M=1 to M=−1 (M=−1 to M=1), $\sigma-$ ($\sigma+$) pulses are necessary. The scale bar is 100 μm

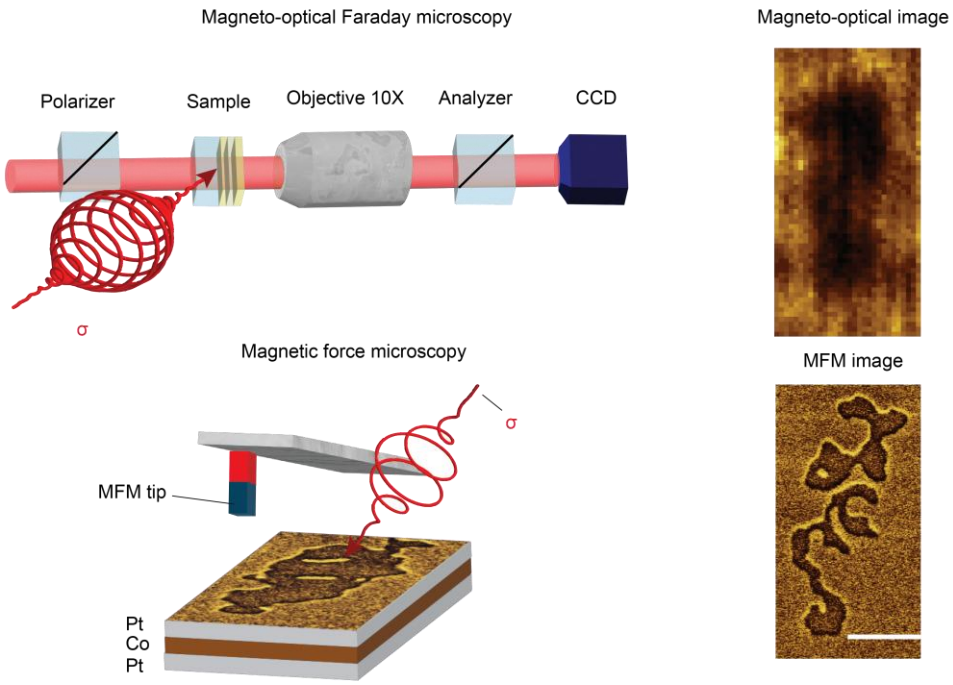

Extended Data Fig. 8 Comparison of magneto-optical Faraday and magnetic force microscopy for studying laser-induced magnetic nanotextures. The Scale bar is 5 μm

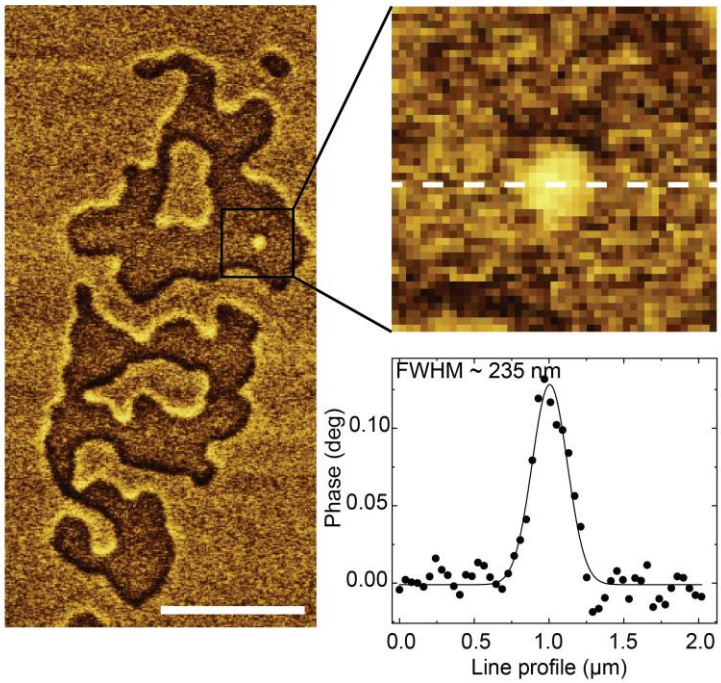

Extended Data Fig. 9 Smallest laser-induced magnetic domain. An MFM image of the laser-induced stochastic domain network was obtained after illumination with six pulses. The zoom-in panel shows the smallest magnetic domain. The line profile was fitted with a Gaussian distribution. The domain size is about 235 nm (Full width at half-maximum). The scale bar is 5 μm

Supplementary Materials: Texture-dependent all-optical switching in ferromagnetic films via stochastic nucleation of nanoscale domains

Dinar Khusyainov[1*], Rein Liefferink[1], MengXing Na[1], Fabian Kammerbauer[2], Robert Frömter[2], Mathias Kläui[2], Dmitry Kozodaev[3], Nikolay Vovk[4], Rostislav Mikhaylovskiy[4], Dmytro Afanasiev[1], Alexey Kimel[1], Johan H. Mentink[1], Theo Rasing[1]

[1*]*Institute for Molecules and Materials, Radboud University, Nijmegen, 6525 AJ, Netherlands.*
[2]*Institute of Physics, Johannes Gutenberg University Mainz, Mainz, 55099, Germany.*
[3]*NT-MDT BV, Sutton 11A, Apeldoorn, 7327AB, Netherlands.*
[4]*Department of Physics, Lancaster University, Bailrigg, Lancaster, LA1 4YW, United Kingdom.*

*Corresponding author. E-mail: dinar.khusyainov@ru.nl;

Supplementary Note I

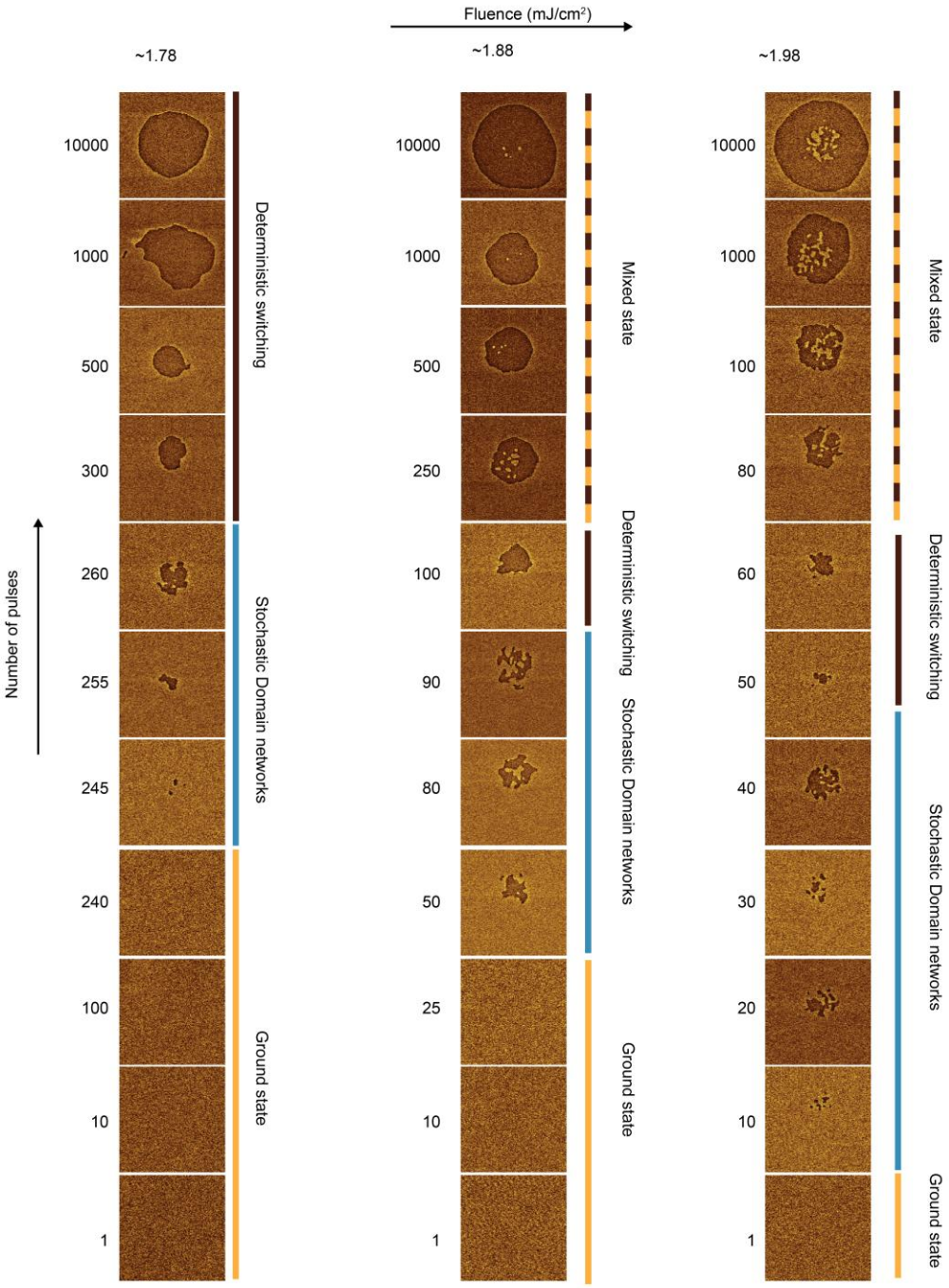

Fig. S1. Original data for the phase diagram of fluence versus the number of pulses in Fig.1b. MFM images of the laser-induced domains in Pt/Co/Pt as a function of fluence and number of pulses. We demonstrate that we observe intermediate states of stochastic domain networks at low-fluence conditions. All images are 30x30 μm². The scale bar is 5 μm.

Supplementary Note II

Using an analytical micromagnetic model, we estimate the switching energy barrier between $M = \pm 1$ of a cell in simulation for all possible configurations of neighbors. We consider a magnetization profile of a square domain of size $s = 200\,nm$, representing the cell, surrounded by domain walls with its four neighboring cells $M_{\mathrm{neighb}} = \pm 1$. To avoid microscopic details, we model the cell switching as an effective 180-degree rotation of its magnetization. In the micromagnetic model, this rotation also affects the magnetization profile of the domain walls with their neighbors. This leads to the neighbor-dependent evolution of the micromagnetic energy during the rotation, from which we extract the switching energy barriers. An example of a magnetization configuration during such rotation is given in Fig. S2. The micromagnetic energy is given by the out-of-plane uniaxial anisotropy and exchange energy

$$E = \iiint K_{\mathrm{eff}}(\boldsymbol{M}\cdot\hat{\boldsymbol{z}})^2 \mathrm{d}x\mathrm{d}y\mathrm{d}z + \iiint A\left(\frac{\mathrm{d}M}{\mathrm{d}x}\right)^2 \mathrm{d}x\mathrm{d}y\mathrm{d}z, \tag{1}$$

where $\boldsymbol{M}$ is the continuous magnetization field, A is the exchange stiffness, and K_{eff} is the effective out-of-plane anisotropy. Note that for simplicity, the dipole interaction is only taken into account as shape anisotropy to avoid long-range terms. It will be useful for the energy calculation to split the configuration into five regions, as indicated in Fig. S2.

The rotation is parameterized by the out-of-plane magnetization $-1 < m < 1$. For $m = -1$ to $m = 1$ domain walls (i.e., between antiparallel domains) in such a micromagnetic system, one finds an analytical solution for the domain wall profile [1] giving only non-zero values for the angle with the out-of-plane axis $\theta_{dw}(x) = 2\arctan\left(\exp(x/\Delta)\right)$, where $\Delta = \sqrt{A/K_{\mathrm{eff}}}$ and x is the distance perpendicular to the domain interface. To accommodate domain walls between $M_{\mathrm{neighb}} = -1$ and arbitrary $-1 < m < 1$, we take an approximate profile

$$\theta_m(x) = 2\arctan\left(\exp\frac{x}{\Delta}\right)\frac{\arccos m}{\pi}. \tag{2}$$

For a wall from $M_{\mathrm{neighb}} = 1$ to m, this becomes $-\theta_{-m}(x)$. For such profiles defined by only one angle $\theta(x)$, the micromagnetic energy density ϵ in the yz-plane can be written as

$$\epsilon = \int K_{\mathrm{eff}}\sin^2\theta(x)\mathrm{d}x + \int A\left(\frac{\mathrm{d}\theta(x)}{\mathrm{d}x}\right)^2 \mathrm{d}x. \tag{3}$$

It is now easy to calculate the exchange energy density for the profile Eq. (2):

$$\epsilon_{\mathrm{dw,exch}}(m) = \int_{-\infty}^{\infty} A\left(\frac{\mathrm{d}\theta(x)}{\mathrm{d}x}\right)^2 \mathrm{d}x = 2\sqrt{AK_{\mathrm{eff}}}\cdot(\arccos(m)/\pi)^2. \tag{4}$$

Note that the profile Eq. (2), in general, never aligns with the anisotropy axis at positive x, so we must bind the extent of the wall to a finite value $x = t = 3\Delta < s/2$ (see Fig. S2). We obtain for the anisotropy energy density in the yz-plane

$$\epsilon_{\mathrm{dw,ani}}(m) = \int_{-t}^{t} K_{\mathrm{eff}}\sin^2(\theta_m(x))\mathrm{d}x \tag{5}$$

$$= K_{\mathrm{eff}}\int_{-t}^{t}\sin^2\left(2\arctan\left(\exp(x/\Delta)\right)\cdot\frac{\arccos(m)}{\pi}\right)\mathrm{d}x, \tag{6}$$

for which no simple analytical solution can be found.

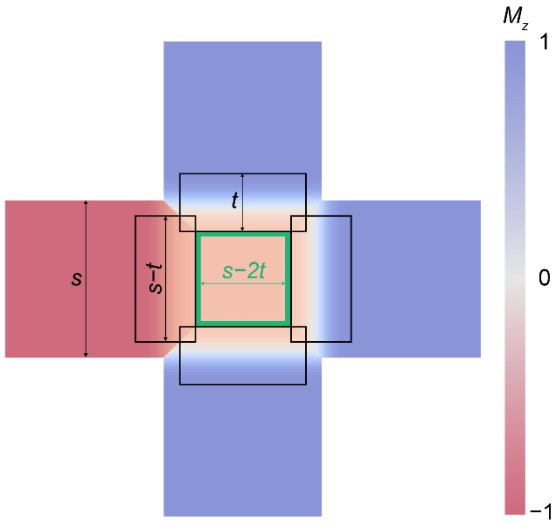

Fig. S2. Example of out-of-plane magnetization configuration under rotation of one model cell with a sketch of the subregions used for the energy calculation. Note that the neighboring domains of the middle cell are fixed at $M_z = M_{\text{neighb}} = \pm 1$. Green and black frames represent the subregions used for the calculations. The subregions correspond to the homogeneous part of the cell (green) and the four domain walls (black).

These expressions hold for the profile from $M_{\text{neighb}} = -1$ to m, but we can write the energy of $M_{\text{neighb}} = 1$ to m walls as $\epsilon_{dw,exch}(-m) + \epsilon_{dw,ani}(-m)$, since the θ only appears inside even functions. These walls stretch along the length s of the domain and its walls, so we take their length as $s - t$. Then, the energy of the four walls is

$$E_{\text{dw}}(m) = d(s-t)\sum_{neighb\ i} \epsilon_{\text{dw,exch}}\,(\text{sgn}(-M_i)m) + \epsilon_{\text{dw,ani}}(\text{sgn}(-M_i)m), \tag{7}$$

where d is the sample thickness.

The exchange energy of the homogeneous part of the domain between the domain walls clearly vanishes, but we still need to calculate its anisotropy energy. On either side, there is a half-domain wall of thickness t, so the remaining anisotropy energy is

$$E_{\text{domain,ani}}(m) = d(s-2t)^2 K_{\text{eff}}(1-m^2). \tag{8}$$

The switching energy barriers are now found from the difference between the peak of the energy during the rotation, i.e., the maximum of $E_{\text{dw}}(m) + E_{\text{domain,ani}}(m)$ for $-1 \le m \le 1$, and the initial energy $E_{\text{dw}}(M) + E_{\text{domain,ani}}(M)$. This gives an approximately linear dependence on the number of aligned (i.e., $MM_{\text{neighb}} = 1$) neighbors n

$$E_b(n) \approx E_0 + E_1 n. \tag{9}$$

We found the best correspondence of the domain shape as well as the fractal dimension for $A/K_{\text{eff}} = \Delta^2 = 285.7\text{nm}^2$, in which case the domain wall thickness is $d_{dw} = \pi\Delta = 53\ nm$. Fitting to equation Eq. (9) then leads to $E_0 = E_1$. Stochastic domain networks and cumulative switching could be achieved for other values A/K_{eff} within an order

magnitude, but the shapes and fractal dimensions deviated from the experimental results. We note that the used value of 53 nm for d_{dw} is a bit large compared to the literature ($d_{dw} \approx 21\ nm$) [2]. Complete quantitative agreement cannot be expected given the approximations made in the analytical micromagnetic model, such as neglecting dipolar and Dzyaloshinskii-Moriya interactions and assuming a classic Bloch domain wall profile.

Supplementary Note III

We present experimental data on the single-pulse laser-induced nucleation of domains in Pt/Co/Pt as a function of pulse width in Fig. S3. We found that decreasing the pulse width results in a reduction of the average sizes of the nucleated domains. The short 100-femtosecond pulse nucleates domains with an average area of approximately 1.1 μm², while the 3 ps pulse nucleates domains with an average area of approximately 3.7 μm². We simulated the single pulse nucleation as a function of the w_{pulse} in our model. The simulations are in agreement with the experiment. According to the simulation, longer pulses should be preferable for helicity-dependent all-optical switching. We note that, experimentally, very long pulse excitation is impossible because the laser's peak intensity must be sufficiently high to reach the Curie temperature without damaging the sample. Due to heat accumulation, excessively long pulses cannot be used for helicity-dependent all-optical switching.

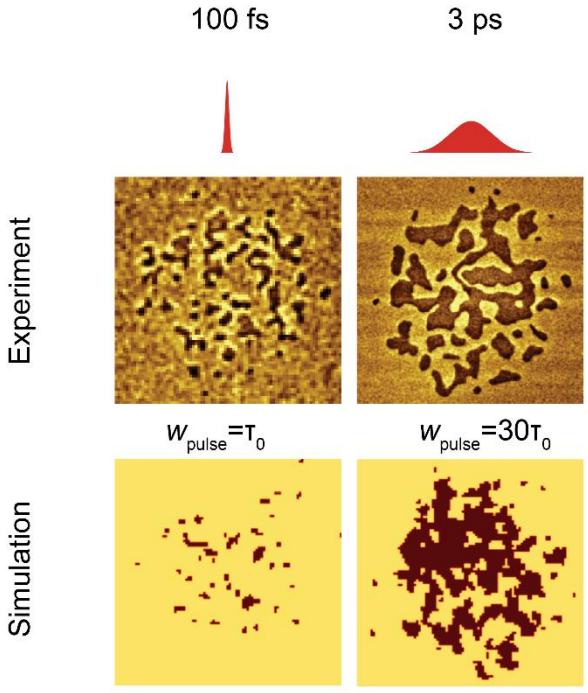

Fig. S3. **Dependence of the size of single-pulse laser-induced nucleated domains on the pulse width**. We plot MFM images and the results of the simulations. We observe that the simulations accurately reproduce the experimental results. The size of the images is 20x20 μm².

Supplementary Note IV

Here we estimate the accumulated temperature in Pt/Co/Pt as a function of the number of pulses. First, we estimate the temperature rise due to the single-pulse laser illumination using the two-temperature model [3]. We use two coupled differential equations:

$$C_e(T_e)\frac{dT_e}{dt} = -G_{el}(T_e - T_l) + P(t), \quad (1)$$

$$C_l(T_l)\frac{dT_l}{dt} = G_{el}(T_e - T_l), \quad (2)$$

where T_e and T_l are the electron and lattice temperatures, C_e is the electronic heat capacity, modeled as γT_e, C_l is the lattice heat capacity, which linearly depends on temperature, G_{el} is the electron-phonon coupling constant, $P(t)$ is the absorbed laser power density a function of time. We perform the transfer matrix method to estimate absorbed fluence in the Pt/Co/Pt trilayer [4]. We plot the absorption profile in the multilayered structure in Fig. S4a. We utilize this data to calculate the absorbed fluence in the Pt/Co/Pt trilayer and to determine the temperature profiles of the electrons and the lattice after being illuminated by a 3 ps laser pulse with a fluence of 2.26 mJ/cm^2. We solve equations (1) and (2) using values for the G_{el}, γ and C_l from reference [3]. We provide the transient electronic and lattice temperature

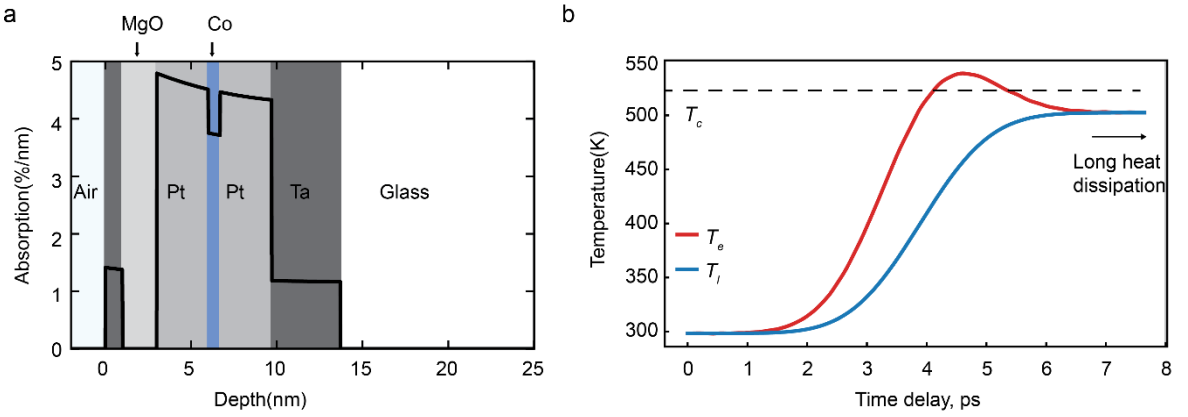

Fig. S4. Evolution of the temperature. (a) Absorption of the 800 nm wavelength light in the whole sample. **(b)** Evolution of the electronic and lattice temperature as a function of the delay time in Pt/Co/Pt trilayer.

profile in Fig. S3 b. The electronic temperature rises on the timescale of half the laser pulse duration, reaches T_c=520 K [2], and peaks at approximately 540 K, followed by relaxation to the lattice temperature over ~ 2 ps, after which it equilibrates with the lattice temperature. Lattice temperature grows right after the laser pulse and levels off at 510 K after ~6 ps. Following long heat dissipation governed by heat dissipation in metal (nanoseconds)[5], and the rest of the heat dissipating in the substrate (milliseconds) [6]. Next, we estimate heat accumulation based on the switched patterns in the Extended Data Fig. 2. We link the threshold electron temperature to the width of the nucleated pattern. The change in the base temperature can be calculated as $\Delta T = T_{th} - T_e(4.5ps)exp\left(-\frac{{w_{th}}^2}{8(FWHM/2.35)^2}\right)$, where T_{th} is a

peak electron temperature at F_T, w_{th} is a width of the switched spot, FWHM is a full width at half maximum of the gaussian beam, which is equal to 110 μm (See Fig. S5a). We show the estimated base temperature increase, ΔT, as a function of the number of laser pulses extracted from an experiment in Fig. S5b. We observe that ΔT increases from approximately 100 pulses to ΔT at around 80 K, followed by subsequent saturation at ΔT at about 120 K. We can estimate the time of the heat dissipation by assuming that heat dissipates exponentially in our sample with time τ. We use the following equation to estimate τ, taking into acount residual heat from previous N pulses: $\Delta T = T_s\left(\exp\left(-\frac{d_{st}}{\tau}\right) + \exp\left(-\frac{2d_{st}}{\tau}\right) + \ldots + \exp\left(-\frac{Nd_{st}}{\tau}\right)\right) = T_s\left(\frac{1-\exp\left(-\frac{d_{st}}{\tau}N\right)}{1-\exp\left(-\frac{d_{st}}{\tau}\right)} - 1\right)$, where T_s is average increase in temperature in the whole sample per pulse, d_{st} is a time separation between pulses. The time constant of the heat dissipation is ~80 ms. The time constant here exceeds that of the sample on Si substrate, which is recorded at 50 ms at room temperature, attributed to silicon's heat conduction [6]. In this instance, the heat conduction of the glass

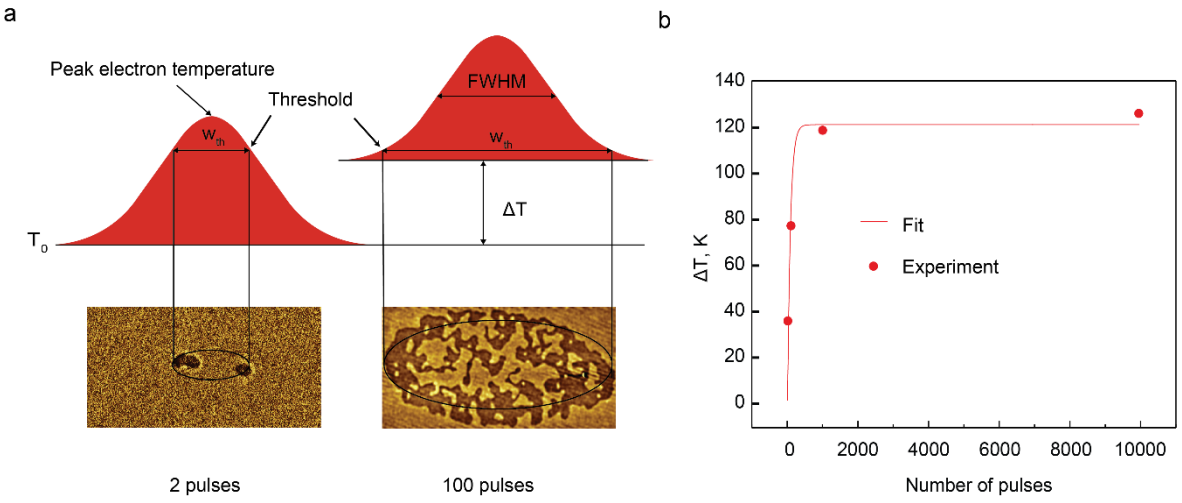

Fig. S5. Estimation of the multipulse heat accumulation. (a) Sketch of the estimation of the heat accumulation procedure. We extract the change in the base temperature T_0 by tracking the change in the threshold temperature relative to the beam FWHM. **(b)** The change in the base temperature as a function of the number of pulses.

substrate is the cause of the slower heat dissipation.

Supplementary Note V

In this note, we estimate the peak temperature at the deterministically switched region after 10 K pulses of illumination with a fluence of 2.26 mJ/cm^2 (Fig. S6 and Fig. S7a). To estimate heat accumulation in this region, we need to consider that the laser beam intensity is distributed according to a Gaussian distribution. We demonstrate this in Fig. S6, where we show the size of the laser beam in comparison with the nucleated domain after multipulse illumination. Using the spatial profile of the beam and estimated heat accumulation after 10K pulses, we plot the heat accumulation profile

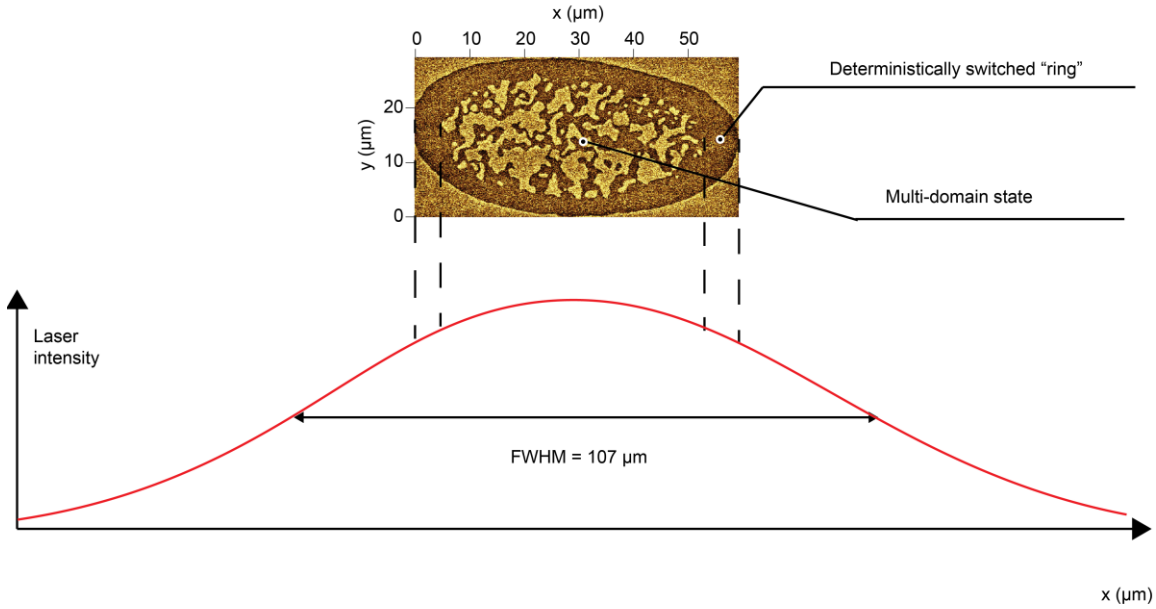

Fig. S6. Laser beam in comparison with laser-induced domains. We plot an MFM image of the laser-induced domains (10,000 pulses and a fluence of 2.26 mJ/cm²) in comparison with a laser beam intensity distribution. The image is to scale.

after illumination with 10K pulses in Fig. S7b. To estimate the peak electron temperature after multipulse illumination, we need to include the temperature profile after single pulse illumination (Fig. S4b). We plot the spatial distribution of a single pulse peak electron temperature in Fig. 7c. We can sum the peak electron temperature and accumulated heat in the deterministically switched region (Fig. 7, black dot), as we consider accumulated heat as a change in the

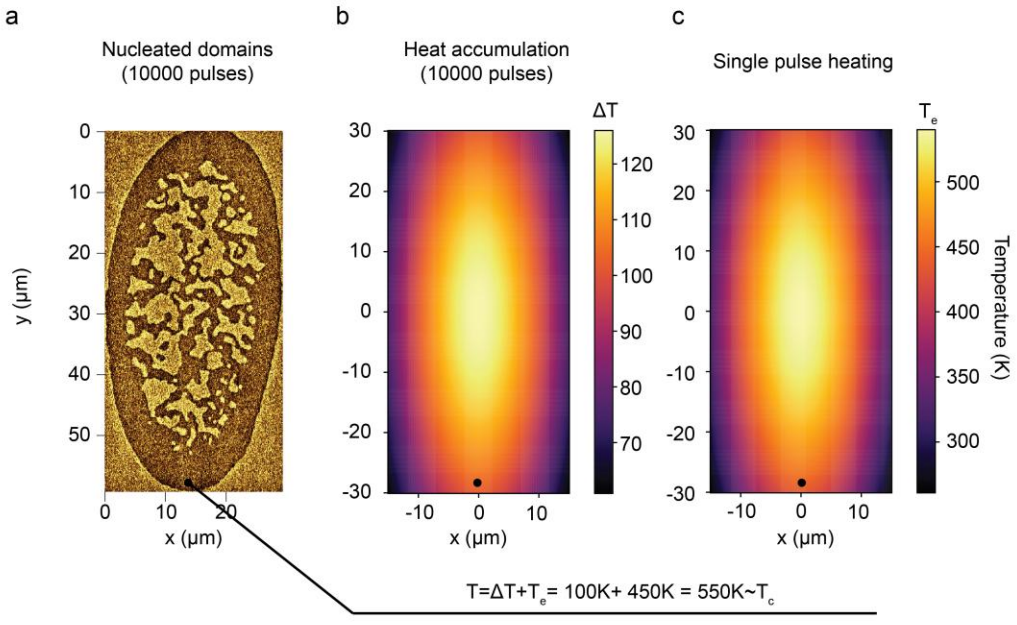

Fig. S7. Peak temperature during multipulse illumination. (a) MFM image of the laser-induced domains after illumination with 10000 pulses **(b)** Spatial distribution of heat accumulation after 10000 pulse illumination. **(c)** Spatial distribution of the single laser pulse peak temperature during illumination. Spatial distribution was calculated taking into account the beam size. Fluence for all the figures was the same (2.26 mJ/cm²)

base temperature. The maximum temperature reached at the deterministically switched ring is ~550 K, which is similar to the peak temperature in the center of the spot after single-pulse illumination (See Fig. S4b). These calculations suggest that texture- and helicity-dependent switching occurs when each pulse in a sequence raises the sample's temperature close to T_c, independent of the number of pulses.

Supplementary Note VI

This note presents an experiment investigating the impact of accumulated heat. We explore how a deterministic state developed by multipulse laser excitation changes with the number of pulses. Each laser pulse in a sequence of pulses is spaced by one second to allow the sample to reset to equilibrium before the next pulse comes (see Fig. S8a). The results are compared with data collected using a 2 ms separation time (see Fig. S8b). In both scenarios, each pulse delivers about 2.2 mJ/cm^2 of fluence. The findings show that with a 1 s separation time between pulses and fewer than 100 pulses, stochastic domain networks form. As the number of pulses increases (greater than 100), these stochastic networks tend to transition toward deterministic switching. For a 2-ms pulse separation, the sample cannot achieve deterministic switching in a high number of pulses regime (>100). The deterministic region shrinks because heat buildup from pulses at the spot center causes a mixed state at high pulse counts. Consequently, the deterministic switching zone moves to fewer pulses (between 25 and 50). This experiment highlights that heat accumulation acts as a parasitic effect. Conversely, accumulated heat can facilitate deterministic switching at fewer pulses, as it boosts the probability of forming complex domain networks and speeds up texture-dependent switching.

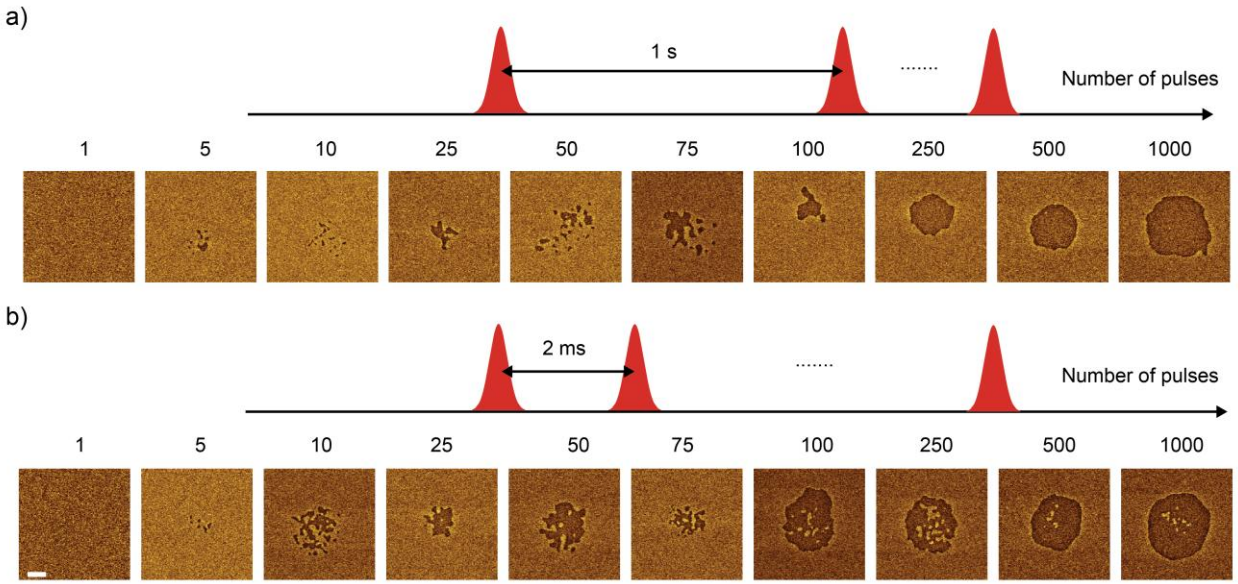

Fig. S8. Effect of the heat accumulation on all-optical switching. MFM image of the laser-induced domains as a function of the number of pulses for a separation time of (a) 1 second and (b) 2 milliseconds between pulses. All images are 30x30 μm². The scale bar is 5 μm.

References

1. On The Theory Of The Dispersion Of Magnetic Permeability In Ferromagnetic Bodies. In: Collected Papers of L.D. Landau. pp. 101–114. Elsevier (1965)

2. Metaxas, P.J., Jamet, J.P., Mougin, A., Cormier, M., Ferré, J., Baltz, V., Rodmacq, B., Dieny, B., Stamps, R.L.: Creep and Flow Regimes of Magnetic Domain-Wall Motion in Ultrathin Pt/Co/Pt Films with Perpendicular Anisotropy. Physical Review Letters. 99, 217208 (2007). https://doi.org/10.1103/PhysRevLett.99.217208

3. Kichin, G., Hehn, M., Gorchon, J., Malinowski, G., Hohlfeld, J., Mangin, S.: From Multiple- to Single-Pulse All-Optical Helicity-Dependent Switching in Ferromagnetic Co/Pt Multilayers. Physical Review Applied. 12, 024019 (2019). https://doi.org/10.1103/PhysRevApplied.12.024019

4. Byrnes, S.J.: Multilayer optical calculations, https://arxiv.org/abs/1603.02720, (2016)

5. Wang, F., Bürgler, D.E., Adam, R., Parlak, U., Cao, D., Greb, C., Heidtfeld, S., Schneider, C.M.: Magnetization relaxation dynamics in [Co / Pt] 3 multilayers on pico- and nanosecond timescales. Phys. Rev. Research. 3, 033061 (2021). https://doi.org/10.1103/PhysRevResearch.3.033061

6. Parlak, U., Adam, R., Bürgler, D.E., Gang, S., Schneider, C.M.: Optically induced magnetization reversal in [Co/Pt] multilayers: Role of domain wall dynamics. Physical Review B. 98, 214443 (2018). https://doi.org/10.1103/PhysRevB.98.214443